Chapter 5
Edge Localized Mode (ELM)

Yunfeng Liang

Abstract The next generation of fusion machines like ITER and DEMO will need a reliable method for controlling the periodic transient expulsion of a considerable amount of energy onto the plasma-facing components caused by instabilities at the plasma edge. The good plasma confinement in these tokamak devices will result in a steepened pressure profile at the plasma edge. When the pressure gradient exceeds a critical value, so-called edge- localized modes (ELMs) are destabilized. These modes feature a periodic fast collapse of the edge pressure, a sudden loss of the confinement, and a subsequent release of heat and particles onto plasma-facing components. The associated transient heat loads might cause excess erosion and lead to a strong reduction of the plasma-facing component lifetime. In this chapter, an overview of recent development of several ELM control methods for next-generation tokamaks, e.g., ITER is given. Some key physics issues related to the mechanism of ELM control are discussed.

5.1 Introduction

The discovery of the high confinement mode (H-mode), which is characterized by the formation of a transport barrier at the edge of the plasma, was made at the ASDEX Tokamak [1]. The transport barrier creates a strong pressure gradient at the plasma edge called the edge pedestal. The H-mode increases the plasma energy confinement time by around a factor of two compared to the Low confinement mode (L-mode). This discovery constitutes a great step towards achieving the higher temperatures and pressures needed to create ignition conditions. The standard tokamak H-mode is foreseen as the baseline operating scenario of a future

Y. Liang (✉)
Forschungszentrum Jülich GmbH, Association EURATOM-FZ Jülich,
Institut Für Energieforschung—Plasmaphysik, Trilateral Euregio Cluster,
52425 Jülich, Germany
e-mail: y.liang@fz-juelich.de

V. Igochine (ed.), *Active Control of Magneto-hydrodynamic Instabilities in Hot Plasmas*, Springer Series on Atomic, Optical, and Plasma Physics 83,
DOI 10.1007/978-3-662-44222-7_5

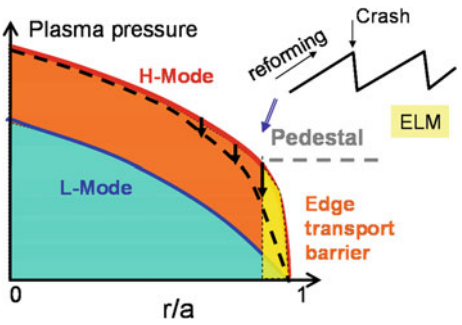

Fig. 5.1 Pressure profiles of L and H- Mode plasmas

fusion machine, e.g. ITER [2]. However, as another consequence of this discovery, a steep plasma pressure gradient and associated increased current density at the edge pedestal could exceed a threshold value to drive magnetohydrodynamic (MHD) instabilities referred to as Edge Localized Modes (ELMs) [1, 3].

In a standard H-mode plasma, ELMs occur repetitively and the edge pedestal collapses towards a shallower pressure gradient within a few hundred microseconds. An expulsion of large amounts of heat and particles onto the plasma facing components from the confined plasma occurs and later the edge pedestal recovers again to a steep gradient, as shown in Fig. 5.1. Each ELM is characterized by an increase in the radiation shown in the D_α line emissions, a burst of magnetic activity. The increase in D_α indicates an increase in edge recycling and can be used to give a measurement of the inward particle flux. ELM events can lead to large transient heat and particle loads on the plasma facing components as well as reducing the pedestal energy confinement by $\sim$10–20 %.

Using results from various current devices, an extrapolation of the heat and particles deposited on the wall components has been carried out for ITER. Since the exact physics and scaling is unknown, the predicted ELM energy loss ranges from $\sim$5 to $\sim$22 MJ. It is expected that approximately half of this energy will reach the wall and be deposited over a region of $\sim$1 m^2, known as the wetted area. Thus, the surface energy density is suggested to be 2.5–11 MJm^{-2} which is $\sim$5–20 times higher than acceptable for the planned first wall components, primarily made of tungsten or carbon fibre composites, which can receive a maximum of 0.5 MJm^{-2}. Therefore, it is important to find mitigation/suppression solutions for ELMs.

The research of ELMs is also of high interest generally, as it involves both linear and non-linear relaxations, requires knowledge of microscopic and macroscopic processes in a volatile plasma with a large magnetic field, and includes higher dimensional effects such as turbulence and 3-dimensional distortions. This understanding enhances similar research into the mechanisms occurring at the edge of stars, for example solar flares.

In this Chapter, a brief introduction on the present common understanding of ELM physics is given in Sect. 5.2. An overview of recent developments of several existing ELM control methods for next-generation tokamaks, e.g., ITER is given in Sects. 5.3–5.5. Some key physics issues related to the mechanism of ELM control are described.

5.2 Physics of Edge Localized Mode in Tokamaks

5.2.1 ELM Types

Edge localized modes have been studied on a wide range of tokamaks including: Alcator C-MOD [4], ASDEX-U [5], COMPASS-D [6], DIII-D [7], EAST [8], JET [9], JFT- 2 M [10], JT-60U [11, 12], MAST [13], NSTX [14], TCV [15], and TEXTOR [16]. The magnetic fluctuations, the short time scales of the ELM growth, and the proximity of the plasma to an MHD stability limit when an ELM occurs, all point towards MHD being able to explain the ELM onset. The phenomenology varies depending on the size and shape of the plasma making it necessary to distinguish between different types of ELM. Connor [3], Suttrop [17] and Zohm [18] have summarized these observations and attempted to create a classification of which the main points will be outlined here.

Three main criteria are used to classify ELMs: the dependence of ELM repetition frequency on the heating power (the energy flux through the separatrix), the occurrence of magnetic precursors, and MHD stability analysis, although reference [18] argues that this third criterion is insufficient across different machines.

- **Type-I ELMs**: The D_α radiation shows large isolated bursts and, therefore, Type-I ELMs are also called 'large' or even 'giant' ELMs. These events occur in regimes which have good confinement but expel a large amount of energy. The repetition frequency of type-I ELMs is $\sim$10–100 Hz. As the heating power is increased, the ELM repetition frequency also increases. The energy loss of a Type-I ELM, ΔW_{ELM}, is also much larger than that of other ELM types, being up to $\sim$20 % of the pedestal energy reported in the international database [19]. Unacceptably high transient heat loads onto the plasma facing components (PFCs) are expected in a burning fusion plasma with a type-I ELMy H-mode [20].
- **Type-II ELMs**: To date, Type-II ELMs [21–24] are observed only in strongly-shaped plasmas, i.e. with high elongation and triangularity of the plasma cross-section. Further, the plasma density needs to be rather high. The magnitude of the ELM bursts is lower and the frequency is higher than that of type-I ELMs, while the confinement stays almost as good. Sometimes, type-II ELMs are called 'grassy' ELMs. Compared with a Type-I ELMy plasma, enhanced magnetic turbulence has been seen in the inter-ELM phase of Type-II ELMy H-mode plasmas. Although Type-II ELMs show potential for steady-state operation of a tokamak with good confinement, and efficient impurity exhaust while not damaging the divertor plates, they appear only in a narrow operational window, and it is still unclear whether Type-II ELMs will be possible to achieve in a burning fusion plasma. On JET, it is hard to establish a stationary pure Type-II ELMy H-mode plasma with a single null configuration, but mixed Type-I/II ELMs are often seen in high triangularity and high density H-mode plasmas.

- **Type-III ELMs**: The bursts are small and frequent. Therefore, another name for type-III ELMs is 'small' ELMs. Type-III ELMs appear when the plasma resistivity is rather high (i.e. the edge temperature is rather low). The ELM repetition frequency is found to decrease with increasing heating power. Although the energy lost in a single type-III ELM is significantly lower than in a type-I ELM, the rather high overall energy transport leads to a stronger degradation of the energy confinement of the plasma compared to other ELM types.

In addition to the three conventional ELM types, there are still other different ELM types, such as compound ELMs, Type-V ELMs, observed in different devices. Several small/no ELM regimes such as EDA (enhanced D_α H-mode), grassy ELM, HRS (high recycling steady), QH-mode (quiescent H-mode), type-II and V ELMs with good confinement properties have been obtained in Alcator C-Mod, AUG, DIII-D, JET, JFT-2 M, JT-60U and NSTX.

Type-II ELMs with small ELM amplitude have been found in DIII-D with a large plasma elongation ($\kappa > 1.8$), a high edge safety factor ($q_{95} \sim 7$) and a high triangularity ($\delta \sim 0.5$) [21]. On AUG and JET, Type-II ELMs have been observed in highly shaped plasmas at high density [22, 25, 26]. The grassy ELM regime has been found in JT-60U at lower collisionality in high poloidal beta (β_p) plasmas with a high δ [27, 28]. The grassy-like ELMs have been also observed in H-mode plasmas with $\beta_p > 1.7$, $q_{95} \sim 7$, and $\delta > 0.4$ on JET and AUG [29, 30]. On NSTX, Type-V ELMs are observed in high density, high performance discharges, and they are characterized by a short-lived $n = 1$ pre-cursor mode rotating counter to the plasma current [31]. All these small ELM regimes show that ELM energy losses are evaluated as less than 5 % of the pedestal stored energy.

The QH-mode regime was originally observed in DIII-D [32] and then also produced in AUG [33], JT-60U [34] and JET [35]. QH-mode plasmas, which do not have ELMs, can be sustained with good confinement levels comparable to those observed in the standard ELMy H-mode. The formation of a strong rotation shear in the edge pedestal is thought to be the key to obtaining QH-mode [34, 12, 36]. EDA H-mode was found in Alcator C-Mod after boronization of the first wall [37]. HRS H-mode, which is similar to the EDA regime, has also been observed in JFT-2 M after boronization [38]. Both EDA and HRS H-mode are characterized by an enhanced D_α signal as a consequence of particle losses due to edge MHD and density fluctuations, such that a steady H-mode can be sustained without ELMs.

The characteristics of edge fluctuations and activities of ideal MHD stability leading to small/no ELMs are summarized in [39]. Some of the small ELM regimes identified at high collisionality, such as EDA, Type V, Type-III and Type-II, have been extended into lower collisionality regimes, of increasing relevance to ITER, in recent years. However, the extrapolation and uncertainty are still large, so it remains unclear whether they can be accessed on ITER.

5.2.2 Understanding Edge Localized Modes

Over the last two decades considerable theoretical work has been performed, both analytically and through modelling calculations, to improve the theoretical background. Ideal MHD modes driven by the steep current and pressure gradients at the edge transport barrier are regarded as the most likely candidates to explain the origin of ELMs. From stability calculations performed on the basis of experimental data three types of ideal MHD instabilities can be expected at the edge transport barrier:

- **Localized peeling modes**, which are driven by the edge plasma current density, do not rely on toroidicity as a drive.
- **Edge ballooning modes**, which are driven by the edge plasma pressure gradient, with largest amplitude on the outboard "bad curvature" side, and very small amplitude on the inboard side.
- **Coupled peeling-ballooning modes**, which are driven by the steep edge pressure gradient and consequently large edge bootstrap current.

5.2.2.1 Localized Peeling Modes

The term "peeling" in literature is first mentioned by Frieman [40] as a test function for the radial displacement which describes the occurrence of an instability when a resonance condition is met, $m - nq_a = 0$ for $m > 1$. The peeling mode is destabilized by the finite edge current density and is dependent on the location of the closest rational surface to the plasma edge in the vacuum. The pressure gradient gives both a stabilising effect through the magnetic shear and a destabilising effect through the bootstrap current. This is essentially the same as the well-known external kink mode. The difference is that the kink mode is driven by the derivative of the parallel current density, whilst the peeling mode is driven by the torque created by a finite value of the current density at the plasma edge and no current in the vacuum region. In addition, the peeling mode has a higher localisation than the external kink due to its sensitivity on the outer rational surface. The effect of the distance from the plasma edge to the rational surface leads to strong dependencies on the q profile and the tokamak geometry. A stability criterion for the peeling mode in a toroidal MHD equilibrium surrounded by a vacuum with a continuous pressure profile is formed in reference [41]. This showed that the peeling modes would theoretically be unstable when the ELMs occur. Manickam [42] also argues that the external kink and the more localized peeling mode are strong candidates for driving ELMs. In terms of experimental evidence, the PBX-M machine observed an MHD precursor to an ELM, identified as an ideal external kink mode [43].

The effect of a divertor on the peeling stability needs to be considered. Theoretically at the separatrix, created by the divertor magnetic topology, $q \rightarrow \infty$.

This will have a large effect on the peeling stability as multiple resonant q values will be covered by the peeling mode. The behaviour of the unstable peeling mode growth rate at the last closed flux surface of the plasma has been examined analytically [44, 45]. Modelling focusing on the X-point region is also being conducted [46, 47]. It was found that although the peeling drive is always present, the growth rate tends to zero and the mode becomes marginal in the presence of the separatrix. However, It is still unclear how the q profile acts in a real world situation and so it is general procedure to use the value of the effective edge safety factor at 95 % of the normalized poloidal flux, q_{95}, for tokamaks with a divertor configuration.

5.2.2.2 Edge Ballooning Modes

The ballooning mode arises from the curvature of the tokamak geometry. Modes with high toroidal mode number n modes, localized around their resonant surfaces, feel different curvature effects as they follow the helical field lines. On the high field side the curvature effect is stabilising, whereas for the low field side the curvature is seen to have a destabilising effect. The average of these effects is found to be stabilising for a plasma with a low pressure gradient. However, if the pressure gradient becomes too high, then the average of the curvature becomes a destabilising drive leading to ballooning modes. The stability of ballooning modes can be approximated from a balance of the driving term from the pressure gradient and the stabilising effect of the energy required for field line bending.

The value of the magnetic shear is also important for ballooning mode stability. At values of high magnetic shear the mode is stabilized. On the other hand, at very low values of shear "second stability access" is granted. This additional region of stability is not an obvious result, as a higher pressure would increase the drive of the ballooning modes. However, at high pressure a strong distortion of the equilibrium magnetic flux surfaces occurs, which increases the local pitch and decreases the shear at the LFS. The increase in the local pitch causes the plasma to spend more time in the good curvature region, which as stated is stabilising. The decrease of the shear creates a large region of negative shear, which apart from being stabilising itself, also pushes the zero shear point away from the LFS to a more stable part of the plasma. The combination of these effects is responsible for the second stability access. This is advantageous not only due to the extra stability granted but also because it produces significant reductions in the required toroidal field and plasma current.

At the edge of the plasma an extra boundary condition must be in place as the ballooning mode can not extend into the vacuum region. This breaks the symmetry of the envelope of influence of the mode on the surrounding surfaces and creates a more localized perturbation. Non-linear ballooning theory [48] suggests that the mode will be broad along the field line but narrow perpendicular to it. As a result the ejected particles will have a filament structure which will narrow and twist to squeeze between adjacent magnetic field lines. This filament is then predicted

to have a radially explosive behaviour but could remain partially connected to the plasma core acting as a conduit for further particles to flow along.

On MAST, during an ELM crash, multiple peaks have been observed in the ion saturation current, measured using the reciprocating Langmuir probe [49], suggesting more than one structure rotating around the plasma. The energy of these structures, calculated from the change of the density profiles, would be small amount ($\sim$ <10 J) and would only account for a fraction of the total ELM energy loss. Thus, these structures must not be isolated blobs but remain partially connected to the plasma and act as a particle conduit, i.e. a filament from core to SOL. These predictions have been verified experimentally on the MAST tokamak [50, 51]. This was found when comparing high resolution Thomson scattering density profiles over an ELM event, which shows that ELMs have little effect on the inboard side but cause a large reduction in the density gradient on the outboard side. Immediately following this density gradient drop, poloidally localized density structures, moving radially away from the plasma, were seen, indicating propagating structures rather than a diffusion of particles. A high speed visible camera backs up these observations showing clear elongated structures along the field lines. Filament structures associated with ELMs have also been observed on ASDEX Upgrade [52].

5.2.2.3 Coupled Peeling-Ballooning Modes

It has been put forward that a spectrum of peeling modes are unstable in the L-mode creating a large amount of anomalous transport [53]. As the plasma enters H-mode the collisionality increases stabilising the majority of the peeling modes, thus reducing anomalous transport; although a few peeling modes may remain marginally unstable. The transport barrier is now formed allowing the pedestal pressure to increase which in turn increases the ballooning stability parameter. When this reaches the ballooning stability limit it can either cause the onset of a ballooning mode, or the plasma can stay on the ballooning stability threshold whilst on a slower diffusive time scale the bootstrap current increases, due to the increasing pressure and decreasing collisionality which would allow a greater trapped particle fraction. When the bootstrap current has risen sufficiently to reach the peeling mode stability threshold, there is a possibility that the harmonics of the unstable peeling and ballooning modes couple, creating a large crash in the pedestal as seen for the large ELMs. Stability analysis of the coupled peeling-ballooning modes has indeed shown the plasma to reach the ballooning boundary and hold there until the peeling instability condition is met before the ELM crash occurs with intermediate toroidal mode numbers [54]. These coupled peeling-ballooning modes are complex and interesting phenomena as the bootstrap current, shear and pressure all play dual roles of stabilising and destabilising. Thus a useful representation of these modes is their potential energy δW for a radial displacement ξ [55]

$$\delta W = \pi \int_0^{\psi_a} d\psi \oint d\theta \left\{ \frac{JB^2}{R^2 B_p^2} \left| k_{||} \xi \right|^2 + \frac{R^2 B_p^2}{JB^2} \left| \frac{1}{n} \frac{\partial}{\partial \psi} \left(JBk_{||} \xi \right) \right|^2 \right.$$
$$- \frac{2J}{B^2} \frac{dp}{d\psi} \left[|\xi|^2 \frac{\partial}{\partial \psi} \left(p + \frac{B^2}{2} \right) - \frac{i}{2} \frac{I}{JB^2} \frac{\partial B^2}{\partial \theta} \frac{\xi^*}{n} \frac{\partial \xi}{\partial \psi} \right] \tag{5.1}$$
$$\left. - \frac{\xi^*}{n} JBk_{||} \left(\frac{\partial \sigma}{\partial \psi} \xi \right) + \frac{\partial}{\partial \psi} \left[\frac{\sigma}{n} \xi JBk_{||}^* \xi^* \right] \right\},$$

where B_p is the poloidal component of the magnetic field B, p is the plasma pressure, $k_{||}$ is the parallel length to the magnetic field over which the displacement varies, R is the radius of curvature $\sim R_0$, the major radius of the torus, and θ, ϕ, and ψ are the toroidal coordinate system.

Here the first two terms are associated with field line bending, the third term calculates the pressure gradient drive including curvature effects, and the last two terms give the current density gradient drive where I is the plasma current, J is the current density, and $\sigma = \frac{I}{B^2} \frac{\partial p}{\partial \psi} + \frac{\partial I}{\partial \psi}$.

Considering each of the two modes individually, (5.1) states clearly the different terms involved. The peeling mode is highly localized at the plasma edge and has little coupling between its Fourier modes, so the field line bending effects disappear. The pressure gradient acts as a stabilising effect when the plasma experiences good curvature, whereas the current drive acts to destabilize the mode. For a ballooning mode quite the opposite is true and it is found that the field line bending term is enhanced by multiple Fourier harmonics coupling over the rational surfaces and thus acts as a stabilising force. In this case the curvature is described as bad. The current gradient drive becomes less important at the large n associated with ballooning modes.

It should be noted that Peeling-ballooning modes are decoupled when the triangularity is increased, since the magnetic shear depends highly on the shape of the plasma cross section, allowing access to second stability. Thus a "Bean" shape poloidal cross section would allow access to the second stability region [56].

5.2.3 ELM Stability Diagram

Although some of the features are common to all ELMs, there are also distinctive differences. Regarding the theoretical peeling-ballooning stability limit, the ELM stability diagram can be summarized as shown in Fig. 5.2. Here, the peeling-ballooning stability limit depends on the maximum value of the normalized pedestal pressure gradient [57],

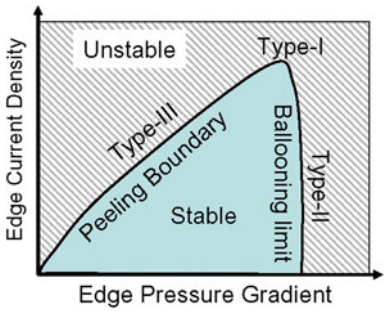

Fig. 5.2 ELM stability diagram

$$\alpha = -\frac{\mu_0}{2\pi^2}\frac{\partial p}{\partial \psi}\frac{\partial V}{\partial \psi}\left(\frac{V}{2\pi^2 R_0}\right)^{1/2}, \tag{5.2}$$

(where V is the plasma volume, p is the pressure, ψ is the poloidal magnetic flux and R_0 is the major radius of the plasma), and a normalized pedestal current density j_N^{ped}, which is taken to be the peak value of the parallel current density in the pedestal region normalized by the average parallel current density in the pedestal. In an H-mode plasma, the edge plasma current density has a substantial bootstrap current component which is parallel to the magnetic field. In a toroidal magnetic confinement system, the momentum transfer between trapped and passing electrons is balanced with that between passing electrons and ions. The bootstrap current, j_b, is generated from the difference in velocity between the passing ions and the passing electrons. This bootstrap current can be expressed as [58]

$$j_b = -\frac{\varepsilon^{1/2} n}{B_\theta}[2.44(T_e + T_i)\frac{1}{n}\frac{\partial n}{\partial r} + 0.69\frac{\partial T_e}{\partial r} - 0.42\frac{\partial T_i}{\partial r}], \tag{3}$$

Here, ε is the inverse aspect ratio r/R of the plasma minor radius (r) to the major radius (R), B_θ is the poloidal magnetic field, and n, T_e, T_i are the plasma density, electron and ion temperatures respectively. A more precise estimation of the bootstrap current can be made by simulating particle orbits [59].

The development of efficient MHD stability codes such as ELITE [60, 61] and MISHKA [62] has allowed detailed quantification of peeling-ballooning stability boundaries [63] and extensive and largely successful comparisons with observation [64–67]. To date, the peeling-ballooning ELM stability diagram has been commonly used to explain the trigger mechanism for those three conventional ELM types. For Type-I ELMs, the edge instability is both pressure and edge current density driven and close to the corner of the peeling-ballooning stability diagram or even beyond it. However, Type-II ELM instability is pressure driven and close to the "ballooning" limit, while Type-III ELM instability is current density driven and close to the peeling limit.

5.3 ELM Control Methods

As described in the introduction section, Type-I ELMy H-mode is foreseen as the ITER baseline scenario [2]. However, Type-I ELMs lead to an unacceptable periodic expulsion of a considerable fraction of the stored energy content onto the PFCs [20]. Therefore, reliable methods for the control of Type-I ELMy power losses and transient peak heat loads on the PFCs are required for ITER. In addition, any acceptable ELM control mechanism should ensure that the plasma is kept in good confinement.

Experimental results from smaller machines have shown that by tailoring the plasma shape and the gas injection, H-mode regimes [22] with small ELMs can be accessed. However, on larger machines such as JET, this is only possible over a limited range of plasma parameters [29]. Active methods of ELM control with the goal of reducing the power loading are therefore required.

To date, investigation of Type-I ELM control is mainly directed into three different strategies:

(i) **Radiating dispersion**: Dispersing the ELM energy loss by radiation before it is deposited at the PFCs.
(ii) **ELM suppression**: stabilizing the ELM instability by means of controlling either the pedestal pressure gradient or the edge current density below the peeling-ballooning ELM stability limit.
(iii) **ELM mitigation**: destabilizing the ELM instability, thus increasing ELM frequency and reducing the ELM energy losses, by applying either steady-state or transient perturbations at the plasma edge.

In the last ten years, several active methods, including (i) radiating divertors (impurity gas puffing) [68–70], (ii) magnetic triggering (vertical kicks) [71], (iii) pellet pace-making of ELMs [72], and (iv) resonant magnetic perturbation (RMP) fields [73, 74], have been developed for Type-I ELM suppression/mitigation.

5.3.1 Radiating Dispersion

Impurity gas seeding is considered as the primary technique for decreasing the inter-ELM heat loads onto the divertor, and large radiation fractions in the SOL and divertor (P_{rad}/P_{out} higher than 0.5 for ITER [75] and 0.9 for DEMO [76], where P_{out} is power exhausted to the SOL) are required. On the another hand, both increases in the ELM frequency and reduction in the ELM peak heat loads onto the divertor, so-called ELM mitigation, have been observed with impurity radiation in a Type-I ELMy H-mode plasma.

5.3.1.1 Type-I ELM Mitigation with Radiative Divertor

On JET, argon and nitrogen have been injected into Type-I ELMy H-modes up to radiative power fractions of 65 % to avoid a transition into Type-III ELMy H-mode or accumulation of argon in the plasma core [77]. The reduction in ELM energy due to radiative dissipation is about 20 % on the outer divertor target and about 25 % on the inner divertor target. Typically the confinement enhancement factor ($H98(y, 2)$) [2] is decreased from 1.0 to $\sim$0.87–0.97, depending on the radiative power fraction and the plasma density [77]. As a consequence the energy deposited onto the divertor target is then decreased. Further increase in the radiative power fractions above 65 % causes a transition from Type-I ELMs to Type-III ELMs [78–80], the so-called radiating Type-III ELMy H-mode, and the plasma confinement becomes even worse ($H98(y, 2) < 0.85$).

In JT-60U, power handling by neon and argon seeding has been investigated in Type-I ELMy H-mode and reversed shear plasmas [81–85]. Good confinement ($H98(y,2) \geq 0.85$) was maintained up to a high density fraction of $\overline{n_e}/n_{GW} \sim 0.8 - 0.9$ (n_{GW} is the Greenwald density) and a high radiation fraction of $P_{rad}/P_{out} = 0.7$–0.9, but it was sustained for only $\sim$2 s in a standard Type-I H-mode plasma, and then radiative collapse occurred. Sustainment of a high radiation for a longer period with impurity seeding has been achieved in ELMy H-mode plasma with an internal transport barrier (ITB). The best performance of the energy confinement of $H98(y,2) = 0.88 - 0.95$ with a large radiation fraction of 0.75–0.95 was obtained for the combination of the Ar and Ne seeding case. Similar to the JET observations, a large radiation loss in the main plasma caused a change in the ELM characteristics from Type-I to Type-III.

5.3.1.2 Open Questions

On JET, to date, a strong radiative dissipation effect with a reduction in ELM energy of more than 50 % is only observed in plasmas with small ELMs ($\Delta W_{ELM} < 25$ kJ) [77, 86]. This experimental observation is consistent with the prediction of edge transport modelling. The calculation results from the edge transport codes EDGE2D/EIRENE [87, 88] show that the nitrogen in the divertor region is ionized to higher ionization stages, which radiate less effectively. For ITER, the modelling by B2-EIRENE [89] predicts that significant radiative dissipation of the large Type-I ELM energy is unlikely. Only for very small ELMs ($\Delta W_{ELM} < 0.6$ MJ), the ELM energy loss is possibly dissipated by impurity seeding on ITER. Therefore, a combination of a radiating divertor with other active ELM control methods is essential for applicability to ITER.

5.3.2 Vertical Kicks

Actively controlled vertical kicks (fast vertical movements of the plasma column with pre-programmed frequency and amplitude) have demonstrated that the ELM frequency can be locked to the frequency of the externally imposed $n = 0$ magnetic perturbation, enabling ELM control (frequency and size). Here, n is the toroidal mode number. The fast modulating $n = 0$ magnetic perturbation is induced by a set of vertical stabilization coils with controllable frequency and amplitude. This method was first developed in TCV [71], and has also been successfully applied in AUG [90], JET [91] and NSTX [92].

5.3.2.1 ELM Control Using Vertical Kicks

In TCV, the fast vertical movement is provoked by the positional control coils inside the vacuum vessel. Experiments on the TCV tokamak showed synchronous modulation of the ELM activity, with ELMs occurring in bursts only during a rapid upward motion of the plasma approaching ~ 1 cm, in a single null Ohmically heated type-III ELMy H-mode plasma [71]. The modulation frequency was around 50 Hz. Phase synchronization was found between the ELM cycle and the external perturbation. The ELM frequency was found to track scans in the external driver frequency about its unperturbed value over a frequency range that increased with the amplitude of the perturbation. It was also found that scaling of the ELM amplitude with the inter-ELM period was preserved in the presence of the perturbation, so that the ELM amplitude could be controlled by altering the ELM period.

On AUG, active ELM control with vertical kicks has now also been demonstrated in the ITER-relevant type-I ELMy regime [90]. The experiments showed the ELM frequency becoming identical to the driving frequency in steady state for an applied motion of only about twice the value caused by an intrinsic ELM event. Figure 5.3 shows a typical example from this experiment. The ELM frequency is raised and locks to the frequency of imposed vertical (position z,$v \equiv dz/dt$) movement of the plasma column. The modest impact of magnetic triggering on particle and energy confinement has been seen when the ELM frequency increases from 43 to 56 Hz. A reduction in ELM-imposed energy losses is not pronounced, which might be due to the small increase in the ELM frequency by a factor of 1.3 only.

On NSTX, scenarios for ELM pacing with rapid vertical kicks induced by external coils have been developed for the first time in an ST plasma [92]. Similar to TCV results, ELMs are most likely to be triggered as the plasma moves up by ~ 2 cm [92]. When the frequency of pre-programmed kicks is set to 30 Hz, synchronization of the ELM cycle with the kicks has been observed. However, when the frequency of the kicks increases to 45 Hz, the ELMs were observed to become quite rapid (~ 60 Hz), though the synchronization with the plasma motion was unclear. These rapid ELMs resulted in a substantial reduction in the per-ELM

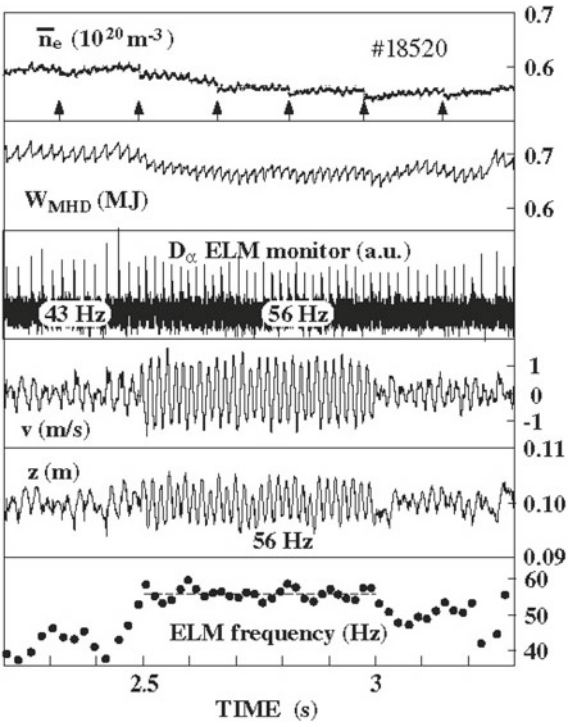

Fig. 5.3 Demonstration of magnetic ELM triggering in a type-I ELMy H-mode. The time traces plotted from top to bottom are line averaged density, plasma stored energy, D_α signal measured from the divertor region, plasma vertical motion velocity and position, and ELM frequency, respectively. The ELM frequency is raised and locks to the frequency of the imposed vertical movement of the plasma column. During the driving phase (2.5–3.0 s) only a modest effect on particle and energy confinement is found. The arrows indicate sawtooth crashes. From [90]

energy loss. Similar to the observation from AUG, the triggered ELMs with a kick frequency of 30 Hz on NSTX show type-I features.

Recently, ELM control with vertical kicks has been successfully applied in JET [91, 93]. The fast vertical movement of the plasma is controlled by the vertical stabilization controller, which has been modified to allow the application of a user defined voltage pulse (so called kick) at an adjustable frequency. Presently, the maximum value of the kick frequency is $\sim$60 Hz due to technical constraints. Similar to the results observed from AUG, JET experimental results show that plasma kicks moving the plasma down towards the X-point can generate high frequency, synchronous ELMs in standard Type-I ELMy H-modes. With an application of the vertical kicks the pedestal density reduces by $\sim$20 % when the ELM frequency is increased from 15 to 40 Hz, while a modest impact on the pedestal temperature is seen. This causes the edge pressure gradient to be reduced. The reduction in ELM size (up to a factor of 3) is accompanied by a minor (<10 %) reduction in the stored energy.

5.3.2.2 Physics and Open Questions

On TCV, DINA simulations showed that when phase locked, the ELMs were found to occur at times when the edge current density was increased under the action of the perturbation, either by direct induction from the changing current in the coil, or by movement of the plasma through the vacuum field [71]. Therefore, it was considered that the ELMs could indeed be driven unstable by the rapid upward motion of the plasma with a modulation of the $n = 0$ magnetic perturbation, attributed to the increased edge current destabilizing the peeling mode (current-driven modes).

However, on AUG, it was found that ELMs were triggered when the plasma downshift velocity reached its maximum, corresponding to the lowest edge current value. The triggered ELMs show clear type-I features. This is the opposite behaviour expected from the peeling-ballooning nature attributed to the ELM boundary and to TCV observations. The reason for this behaviour is not yet clear.

On JET, it was found that a minimum kick size is necessary for the trigger to occur [94]. Successful ELM triggering is obtained in JET with displacements of the current centroid $\sim$0.5–1.5 cm and velocities of the order of 5–10 m/s. Those values still remain less than twice the plasma displacement caused by intrinsic ELMs. However the fast plasma movement is not the only requirement for the ELM to be triggered. For similar pre-programmed kicks the plasma response also depends on the local plasma parameters. Typically 2–3 ms delays are observed between the start of the kick and the ELM and the delays are slightly higher for plasmas with higher pedestal temperature. An increase in the edge temperature will increase the current penetration time. This observation indicates that the modification of edge currents by the induced field and/or change in the plasma equilibrium might be the possible role for the ELM trigger. The sign of the induced edge current perturbation during vertically downward kicks is still under investigation on JET. To date, the precise physics mechanism is still unknown.

5.3.3 Pellet Pace-Making

Shallow injection of pellets has been thought to be a tool for increasing the Type-I ELMs frequency to the pellet injection rate, so called pellet pace-making of ELMs, and consequentially reduce the power load per ELM on the divertor target. Following pioneering experiments on AUG [95], this method has been also studied on JET [96] and DIII-D [97], and it is considered as one potential tool for ITER ELM control [98]. Recently, the first results of ELM pacing using small spherical lithium granules injected mechanically into H-mode discharges were reported on EAST [99].

5.3.3.1 ELM Control Using Frozen Pellet Injection

On AUG, the feasibility of ELM control by continuous injection of small frozen deuterium pellets from the high field side into H-mode discharges has been demonstrated [95]. Two examples with (#15420) and without (#15520) pellet injection are shown in Fig. 5.4. In this experiment, a pellet velocity of 560 m/s and a size of about 6×10^{19} D-atoms were selected. To avoid over-fuelling of the core plasma, a moderate repetition rate close to 20 Hz was chosen. It was found that the ELM frequency was increased and controlled to the imposed pellets injection frequency. Moreover, the impact of the high frequency triggered ELMs on plasma density and stored energy is obviously smaller.

On JET, ELM control experiments with pellet injection were performed. The pellet size was ~ 4 mm (about 4×10^{21} D atoms), and the injection velocities were 150–300 m/s. Although this pellet injector was not originally designed for ELM pacing, the preliminary experimental results demonstrated that prompt triggering of ELMs by pellet injection takes place on a relatively large device [96]. It was found that despite the fuelling effects of the large pellets, ELMs are triggered at any time in the ELM cycle. The pellet triggered ELM appears not to be different from an intrinsically occurring one in terms of energy loss. Experimental results also show that only a small fraction (less than 1 %) of the fuelling pellet mass is ablated when

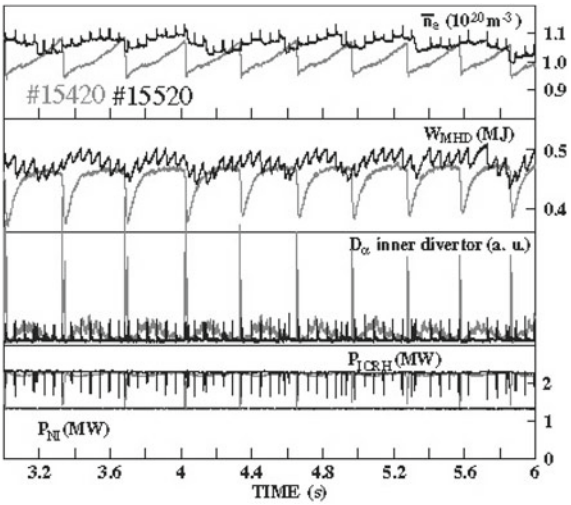

Fig. 5.4 Global temporal evolution of identical discharges without (#15420, *grey*) and with (#15520, *black*) pellet forced ELM control on AUG. The time traces plotted from top to bottom are line averaged density, plasma stored energy, D_α signal measured from the inner divertor region, and heating power from ICRH and NBI. A low frequency (~ 2 Hz) modulation of the plasma stored energy appears in the discharge with pellets injection. This corresponds to slow periodic core profile variations (this is not directly due to sawteeth, the frequency of sawteeth is slightly above 19 Hz in this discharge). The driving mechanism of this phenomenon appearing in the pellet ELM-pacing phase is not yet understood. From [95]

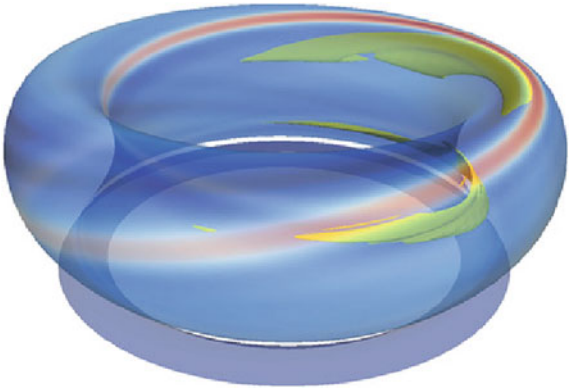

Fig. 5.5 The temperature on a flux surface just inside the separatrix. The density contour of twice the central density is shown in *yellow*. The initial density perturbation was injected into the pedestal on the *left-hand side* in the figure. From [101]

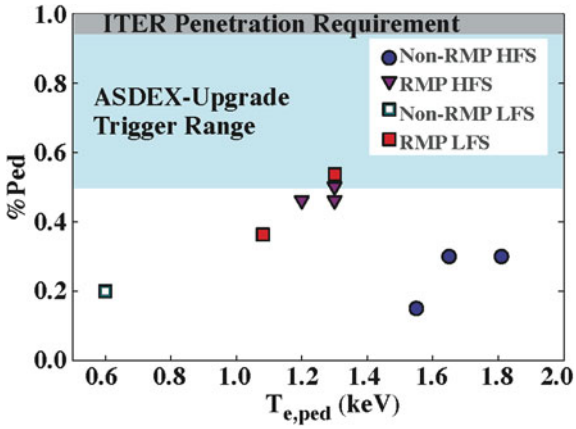

Fig. 5.6 The pellet position where an ELM is triggered, plotted as a fraction of the pedestal height, versus the pedestal temperature measured from DIII-D discharges. All the pellets are 1.8 mm and injected from either the inner wall (HFS) or outside midplane (LFS). From [97]

an ELM is triggered. However, a reduced pellet mass is expected to cause a reduced ablation rate. The JET experimental results also demonstrate the benefits of high field side pellet injection: the penetration to the pedestal top is achieved with a lower pellet mass [96].

Recently, pellets ELM pacing has been applied for an ITER-like shape H-mode plasma on DIII-D. In this experiment, deuterium pellets are injected with a frequency of 14 Hz by alternating pellets between two barrels (one from vertical port at the LFS and one from outside midplane). It was found that an ELM can be triggered as a local event and occurs just as the pellet reaches the separatrix

(± 1 cm) [100]. With pellet injection, the ELM frequency increases by a factor of 5 from 5 to 25 Hz. ELM energy losses were reduced from ~10 to ~3 % of total stored energy with this increase in ELM frequency. The resulting ELM frequency was larger than the pellet frequency. This indicates both a direct ELM trigger by each pellet and an indirect effect on the overall pedestal stability to ELMs from the multiple pellets. In comparison with the non pellet case, the energy confinement time was reduced by ~10 % in the case with pellet paced ELMs. No plasma density increase from the pellets was observed.

5.3.3.2 Physics of Pellet Pace-Making

Progress in understanding the physics of pellet-triggered ELMs is emerging from simulations using the nonlinear MHD code, JOREK [101]. The simulation of pellets injected into the H-mode pedestal shows that high pressure develops in the high density plasmoid, in this case the maximum pressure is ~5 times the pressure on axis. There is a strong initial growth of the low-n modes followed by a growth phase of the higher-n ballooning-like modes. The coupled toroidal harmonics lead to one single helical perturbation centred on the field line of the original pellet position as seen in Fig. 5.7, and there is some experimental evidence for this from JET [102] and AUG [103].

On AUG, it has been observed that ELMs were triggered in less than 200 μs after pellet arrival at the plasma edge. Only a fraction of the pellet had been ablated, forming a rather localized, three-dimensional plasmoid, at the time an ELM was triggered. The localized plasmoid drove the edge unstable well before the deposited mass was spread toroidally. The most probable location of the seed perturbation was found to be at the middle of the pedestal, where the plasma pressure gradient is large. The experimental results also show that the MHD signature of the ELMs appeared about 50 μs after the pellet reached the seed position [103].

On DIII-D, ELM pacing with fuelling-size pellets (containing 2×10^{20} atoms) has been achieved [97]. In this experiment, the fuelling pellets can be injected from either the high field side (HFS) or the low field side (LFS) with a slow speed of 100–150 m/s [104]. The pellet position, where an ELM was triggered, is plotted as a function of the pedestal temperature in Fig. 5.6 for some different operational conditions. Here, the pellet location is defined as a fraction of the pedestal height. It has been found that the ELMs can be triggered well before the fuelling pellet reaches half way up the pedestal. This result is somewhat in contrast to the observations from AUG where the most probable location of the HFS injected pellets to trigger an ELM was found to be at the middle of the pedestal [103].

5.3.3.3 Open Questions

Further experiments on AUG also demonstrated that over-fuelling of the core plasma with either a high pellet injection frequency or a large pellet size could

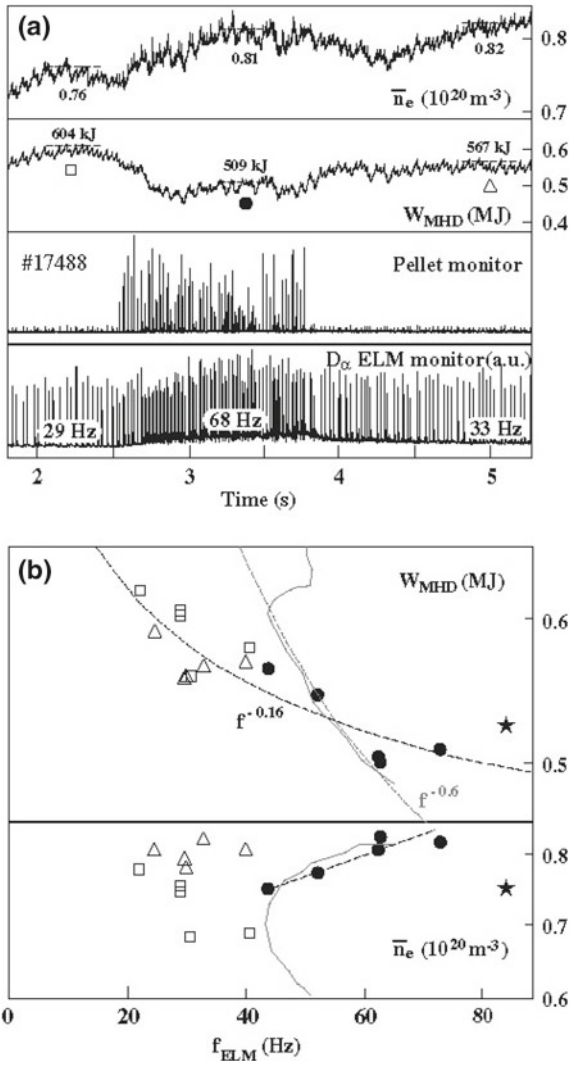

Fig. 5.7 **a** Temporal evolution of plasma density, stored energy, pellet and ELM monitor signals in a type-I ELMy discharge containing a pellet pace-making sequence (averaged ~68 Hz) and fuelling rate of $\sim 17 \times 10^{20}$ D/s. **b** Data compiled from a pellet injection frequency scan showing a mild degradation of confinement with increasing ELM frequency for pellet pace-making. From [72]

cause increasing the convective energy losses and then impact on the energy confinement [72]. One example from this experiment is shown in Fig. 5.5. A clear increase in the density was observed in the pellet injection phase. Reduction of the stored energy and increase in ELM frequency with respect to the pre-pellet phases is visible. Hence, optimization of the pellet size to avoid over-fuelling is important for ELM control with pellet pace-making. These results also indicate that shallow injection is needed for ELM pacing. On the other hand, it is still to be proven whether the concept will work for bigger machine sizes.

On DIII-D, a pellet dropper has been developed for testing the ability of small slow pellets to achieve ELM pacing [105]. The pellet dropper has obtained a

50 Hz injection rate and a 1 mm pellet size. Since pellets are dropped into a funnel that guides them into a tube directed to the top of the plasma using gravity as the accelerator, it results in slow injection speed, <10 m/s, to minimize penetration into the core plasma. Initial results with the pellet dropper indicate that fast ions deflect the pellets toroidally before penetrating deep enough to trigger ELMs [97]. However, a pellet dropper type device might be difficult to apply in ITER due to lack of vertical injection/dropping ports. Future experiments from the dropper on DIII-D will help to investigate the optimized pellet size and speed needed to trigger ELMs reliably in ITER.

In addition, a question, whether alternative materials for pellets could be used for ITER ELM control, is under consideration. On EAST, ELMs have been triggered successfully and in a controlled manner using low velocity Li granules during H-mode discharges [99]. Triggering of ELMs was accomplished using a simple rotating impeller to inject sub-millimeter size granules at speeds of a few tens of meters per second into the outer midplane of EAST. During the injection phase, ELMs were triggered with near 100 % efficiency. A wide range of granule penetration depths was observed, and a substantial fraction of the injected granules appeared to penetrate up to 50 % deeper than the nominal EAST H-mode pedestal width. This result confirmed that ELMs can be triggered using the injection of something other than frozen hydrogenic/deuterium pellets and allows for the contemplation of lithium or beryllium-based ELM pace-making on future fusion devices.

With respect to ITER, the pellet pace-making of ELMs is still to be investigated in the relevant parameter region of, e.g. lower collisionality or much higher pedestal temperature. In addition, an enhancement factor of the intrinsic ELM frequency by a factor of almost 20 is necessary. On the other hand, synergism of pellet fuelling and external ELM triggering seems quite possible. Using low-Z impurity pellets would allow for the decoupling of the ELM-triggering process from the plasma-fuelling process. Indeed, pellet pace-making might assist other ELM control techniques, helping to compensate the density pump-out caused by RMP ELM control/suppression.

5.3.4 Resonant Magnetic Perturbation Fields

Active control of ELMs by RMP fields offers an attractive method for next-generation tokamaks, e.g. ITER. The results obtained from DIII-D, JET, MAST, KSTAR, AUG and NSTX tokamaks have shown that magnetic field perturbations can either completely suppress ELMs [73], trigger small ELMs during ELM free periods, or affect the frequency and size of the type-I ELMs in a controllable way, preserving good global energy confinement [74, 106, 107].

5.3.4.1 Type-I ELM Suppression with RMPs

The first successful demonstration of the ELM suppression technique was reported from DIII-D, where the in-vessel coils (I-coils) have been employed. The I-coils consist of 12 single-turn loops, six above and six below the midplane (up-down symmetric) mounted on the low field side of the vessel. For the ELM suppression experiments, the upper and lower loops are operated with either the same current polarities (even parity) or opposite current polarities (odd parity), and induce a static perturbation field with a toroidal mode number n = 3.

On DIII-D, the experimental results show that the effectiveness of ELM suppression with n = 3 fields depends on q_{95} as well as plasma edge collisionality. In high collisionality ($\nu_e^* \approx 1$) H-mode plasmas [108], Type-I ELMs are suppressed and replaced by small intermittent events with a coherent amplitude modulation of 130 Hz during the application of odd parity n = 3 fields. In low collisionality ($\nu_e^* \leq 0.2$) H-mode plasmas, ELM suppression without small intermittent events is obtained with either even or odd parity n = 3 fields. To date, ELM suppression in those experiments on DIII-D is only observed in a narrow q_{95} window ranging from 3.5 to 3.9 with an even parity n = 3 field and $\sim$7.2 with an odd parity n = 3 field. Outside this q_{95} range Type-I ELMs are mitigated (ELM frequency increased and ELM size decreased) by the applied n = 3 fields. These results indicate a resonant condition on the amplitude of RMPs for ELM suppression.

Furthermore, ELM suppression with n = 3 fields has been also observed in an ITER similar shaped (ISS) high triangularity ($\overline{\delta} = 0.53$) plasma with ITER relevant collisionalities $\nu_e^* \leq 0.2$ [109]. An example discharge with a q_{95} scan from this experiment is shown in Fig. 5.8. ELM suppression with an n = 3 field was observed within a resonant q_{95} window from 3.52 to 3.62. In comparison with a low trangularity ($\overline{\delta} = 0.26$) plasma, the width of the resonant q_{95} window, Δq_{95}, for ELM suppression is reduced by a factor of 3 from 0.3 to 0.1 in ISS plasmas. No clear shift of the resonant q_{95} window was observed between low and high triangularity plasmas. The ELM suppression threshold, which is defined as the minimal coil current required to suppress ELMs, increases by $\sim$25 % in ISS plasmas with respect to that in low δ plasmas. With a vacuum assumption (no plasma response to the perturbation fields taken into account), the width of the island overlap region ($\Delta\Psi$) at the plasma edge has been calculated for an ISS case and a low δ case. It was found that the width of the island overlap region required for ELM suppression is the same. However, 25 % more I-coil current is needed to achieve this width in the ISS plasma. This is mainly due to the edge magnetic shear being higher in the ISS plasma (Figs. 5.9, 5.10 and 5.11).

Suppression of Type-I ELMs has also been established at high collisionality in many other devices, including AUG using an internal off mid-plane coil set (called B-coils) [110], KSTAR using a resonant n = 1 perturbation [111], and JET with the ITER-like wall (ILW) and an n = 2 perturbation [112]. The remaining small ELMs observed in those experiments have negligible ELM energy loss and ELM-peak heat flux onto the divertor plates.

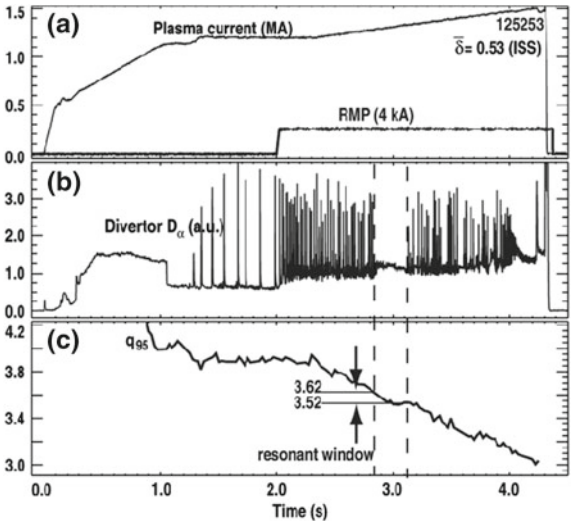

Fig. 5.8 **a** Plasma and I-coil current, **b** lower divertor D_α signal showing ELM suppression window and **c** q_{95} resonant window during a 4 kA RMP pulse in an ITER similar shape plasma with an average triangularity of 0.53 from a DIII-D ELM control discharge (#125253). From [109]

It should be noted that although the suppressed ELM state in high density/collisionality on AUG has many similarities to that observed in DIII-D, the access conditions are significantly different. First of all, type-I ELM suppression can be obtained with n = 1, 2, and 4 magnetic perturbations that are either resonant or non-resonant with a wide range of q_{95} on AUG [113]. The lack of ELM mitigation at n = 0 indicates that a helical perturbation is required, however, there is no apparent correlation with the amplitude of the resonant field component. Secondly, there is a window in edge density in which both resonant and non-resonant magnetic perturbations lead to type-I ELM suppression on AUG [110].

On JET, with a carbon first wall, no clear effect of either n = 1 or n = 2 fields on the ELMs was observed at high collisionality [114]. However, with the ILW suppression of type-I ELMs with an n = 2 perturbation has been achieved [112].

5.3.4.2 Type-I ELM Mitigation with RMPs

Experiments on JET have shown that type-I ELMy plasmas can be actively controlled by the application of static low n = 1 or 2 external magnetic perturbation fields produced by four external error field correction coils (EFCCs) [115] mounted far away from the plasma between the transformer limbs [74, 114, 116, 117]. An overview of a JET ELM control pulse is shown in Fig. 5.12. In these experiments, a type-I ELMy H-mode plasma with a high triangularity shape ($\delta_U = 0.45$ and $\delta_L = 0.4$) was sustained by neutral beam injection. The electron collisionality at the pedestal is ~ 0.2. The Chirikov parameter calculated using the experimental parameters and the vacuum approximation of the perturbation field is about 0.85 at $\Psi^{1/2} = 0.95$. During the EFCC phase the D_α signal measuring the

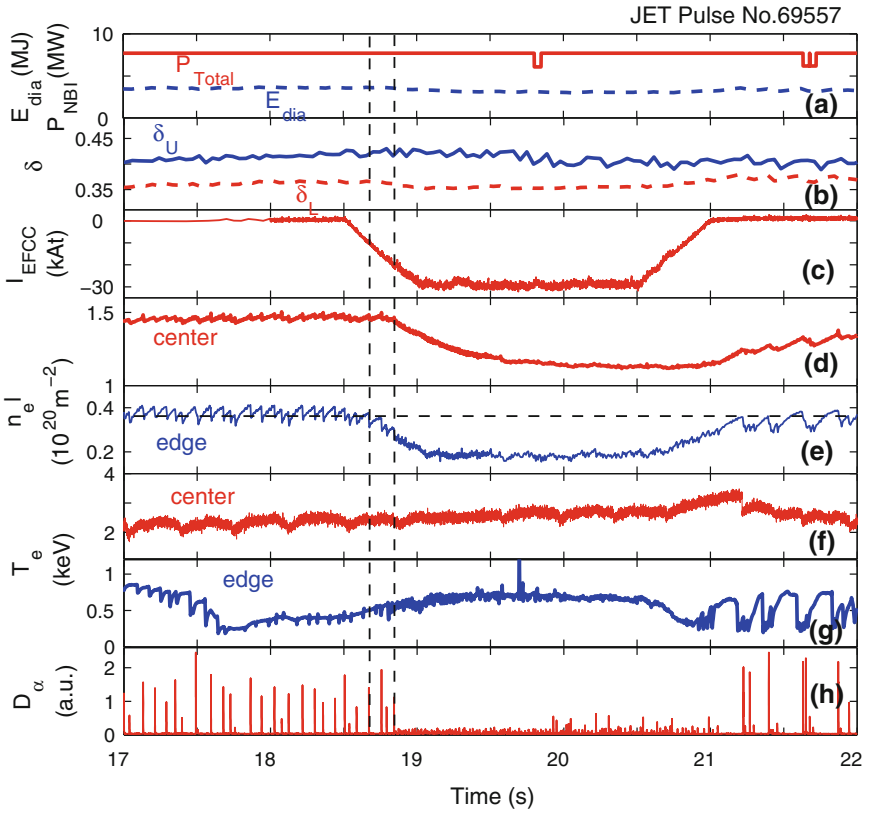

Fig. 5.9 Overview of a typical ELM control experiment on JET. The traces are **a** the total input power, P_{Total}, and the total stored energy, E_{dia}, **b** upper and lower plasma triangularity, δ_U, δ_L, **c** EFCC coil current, the line-integrated electron densities $n_e l$, measured with an interferometer along two lines of sight, **d** one close to the magnetic axis and **e** the other near the pedestal top, electron temperature **f** in the core and **g** near the pedestal top, **h** the D_α signal measured at the inner divertor. From [114]

ELMs showed a strong reduction in amplitude. The ELM frequency increased from $\sim$30 to $\sim$120 Hz, while the periodic energy loss due to the ELM crashes normalized to the total stored energy, $\Delta W/W$, measured by a fast diamagnetic loop, indicates a strong reduction from $\sim$8 % to values below the noise level (<2 %) of the diagnostic. A modest drop (a few per cent) in the total stored energy has been observed during the ELM control phase with the EFCCs. However, when normalized to the $IPB98(y,2)$ scaling the confinement time shows almost no reduction.

Reduction of both the peak particle and heat fluxes during the ELM crash has been observed in ELM control experiments with the application of an n = 1 field on JET [114, 117, 118]. The heat fluxes were measured by Langmuir probes embedded in the divertor tiles and a fast IR camera viewing the divertor target

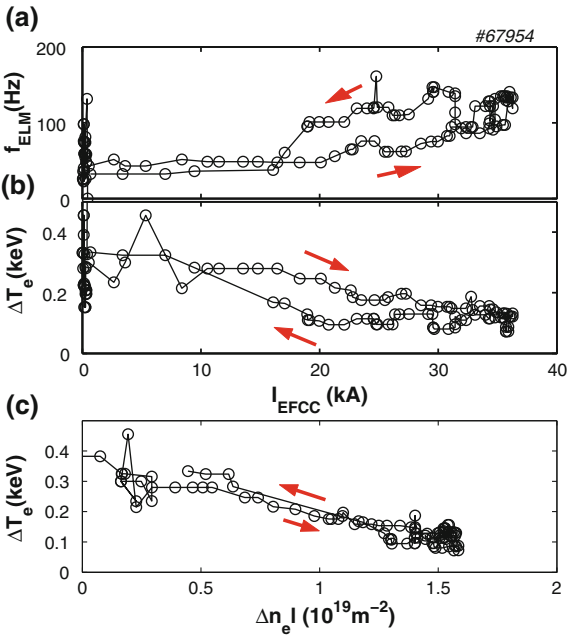

Fig. 5.10 **a** Frequency of the ELMs, f_{ELM}, and **b** the amplitude of ΔT_e as a function of I_{EFCC}. **c** Dependence of ΔT_e on the density drop due to the pump-out effect. From [74]

plates. The reduction in heat flux is mainly due to the drop in particle flux rather than the change in the electron temperature. A reduction in the particle flux has also been observed on the outboard limiter. The fraction of ELMs with a larger particle flux reduces significantly, which benefits the life time of the JET limiter. In addition, a clear reduction of the amplitude of the ELM spikes in the total radiation signal measured by bolometry during ELM mitigation with an n = 1 field has also been observed. These results can be explained in the case of less erosion of carbon from the target when the ELM size is reduced by means of application of the n = 1 field.

JET experimental results also demonstrate that ELM frequency and size can be actively controlled by adjusting the amplitude of the perturbation field/coil current [74]. The dependence of both, f_{ELM} and the amplitude of ΔT_e, on I_{EFCC} is shown in Fig. 5.13. This dependence is found to be different between ramp-up and ramp-down of I_{EFCC} which could be due to a hysteresis effect or the non-stationary nature of the experiment.

Active control of type-I ELMs with n = 1 fields has been developed toward more ITER-relevant configurations and parameters in a wide operational space of plasma triangularity (δ up to 0.45), q_{95} (3–4.8) and normalized beta (β_N up to 3.0) [116, 119] on JET. A similar wide operational window of q_{95} has also been obtained for ELM control with n = 2 fields [116] on JET.

ELM control is also seen with n = 2 fields from external coils in MAST and with n = 3, 4 and 6 fields from in-vessel coils in MAST [106] and with n = 3 fields in DIII-D [120]. On MAST, an increase of the ELM frequency from 500 to

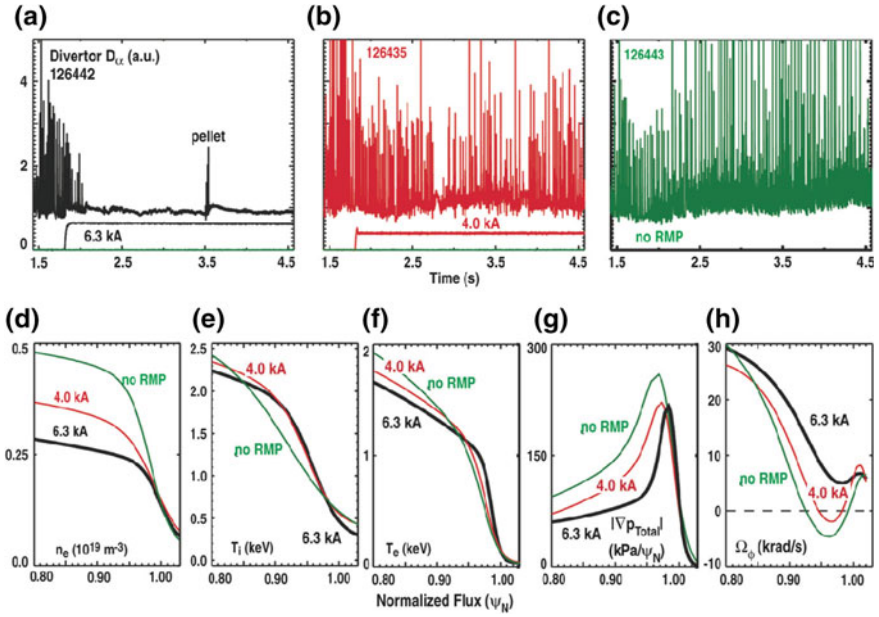

Fig. 5.11 Lower divertor D_α signals showing the ELM characteristics in similar ISS plasmas with n = 3 I-coil currents of **a** 6.3 kA, **b** 4.0 kA and **c** 0 kA. Pedestal profiles showing the **d** density, **e** ion temperature, **f** electron temperature, **g** absolute value of the total pressure gradient and **h** C6 + toroidal rotation for the three I-coil currents (6.3, 4.0 and 0 kA) shown in **a**, **b** and **c**. From [109]

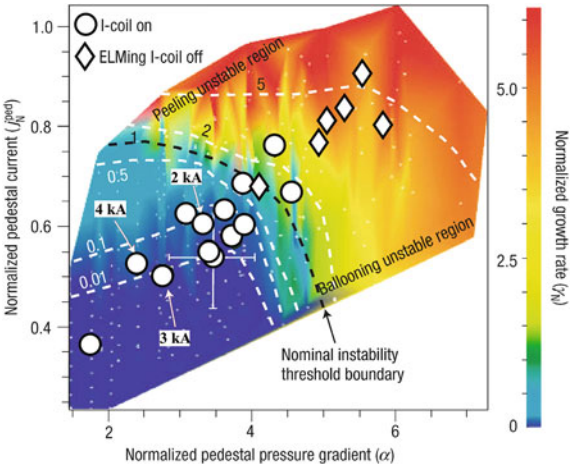

Fig. 5.12 The normalized Peeling-Ballooning mode growth rates of an ELM unstable H-mode plasma (*diamonds*) and RMP-induced ELM-free (*circles*) plasma. From [73]

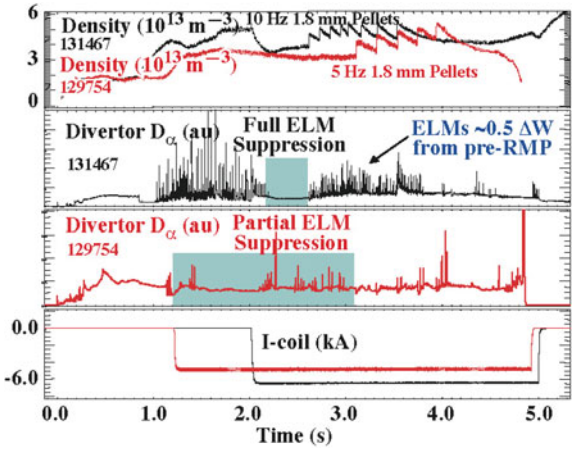

Fig. 5.13 Two cases of 1.8 mm fuelling pellets injected from the inner wall into H-mode plasmas with RMP applied. The time traces plotted are plasma density (*top row*), D_α signals (the *second* and the *third rows*), and currents applied in I-coils (*bottom*). In the fully ELM suppressed case (no. 131467) with 10 Hz pellets, frequent ELMs are observed after the pellets start. The partial ELM suppression case ((no. 129754) with a lower coil current) shows only a few ELMs with the 5 Hz pellets. From [97]

700 Hz has been observed during the application of n = 2 fields induced by the external coils. In this experiment, the Chirikov parameter is greater than 1 where $\sqrt{\Psi_{pol}} > 0.91$, i.e. the region of flux space from the edge of the plasma that is thought to be stochastic satisfies $\Delta\Psi_{pol} > 0.17$ based on vacuum field calculations.

On DIII-D, outside the q_{95} resonance window or below the RMP amplitude threshold for ELM suppression, the DIII-D results show that Type-I ELMs are mitigated. The q_{95} operating window for ELM control with n = 3 fields on DIII-D appears to be much wider than for ELM suppression.

An additional advantage of RMP coils is that they could also provide a technique for ELM pacing. Experiments on NSTX show reliable ELM triggering each time the n = 3 RMP coil current is pulsed, with no apparent loss of stored energy [121]. Similar results are also observed on DIII-D, which demonstrates that a factor of two increase in the ELM frequency can be achieved. However, at higher ELM frequencies, it appears that the triggered ELM energy loss is not inversely proportional to the ELM frequency.

5.3.4.3 RMP Effects on the Pedestal Profiles and Stability

RMP effects on the pedestal profiles have been studied in order to compare ELM suppression with stability theory on DIII-D [109]. Figure 5.9 shows a comparison of the ELM behaviour and pedestal profiles with various I-coil currents in ISS plasmas.

ELM suppression was observed in the case with an I-coil current (I_{coil}) of 6.3 kA, while ELM mitigation was obtained in the case with $I_{coil} = 4$ kA. Reduction of the plasma density (so called density pump-out) has been observed with the application of n = 3 fields. The amplitude of the density drop depends on I_{coil}, and it is ~40 % with $I_{coil} = 6.3$ kA and ~25 % with $I_{coil} = 4$ kA. The change in ion temperature is most pronounced when I_{coil} goes from 0 to 4 kA, however, the bifurcation of the ELM suppression occurs when I_{coil} steps up from 4 to 6.3 kA. The maximal pedestal pressure gradient reduces by 20 % in both $I_{coil} = 4$ kA and $I_{coil} = 6.3$ kA cases, but the pedestal pressure gradient profile becomes narrow with increasing I_{coil}. The plasma edge toroidal rotation increases in the co-current direction with each step increase in I_{coil}, and the most pronounced change was observed when I_{coil} increased from 4 to 6.3 kA. An analysis of the edge pedestal stability shows that the modification of the pedestal pressure profile with application of n = 3 fields moves the pedestal into a stable peeling-ballooning mode operating region as seen in Fig. 5.10 [73]. This observation indicates that ELM suppression with RMP fields occurs due to a direct effect of the RMP on the plasma edge transport rather than an interaction with the ELM eigenmode.

On JET, the electron density at the pedestal top decreased by ~20 % due to the so-called density pump-out [122] during the application of the n = 1 field, while the pedestal electron temperature increased keeping the pedestal pressure almost constant. However, the pedestal pressure gradient obtained from the derivative of the fitted curve shows that the maximum pressure gradient in the profile is decreased by 20 % during the application of the n = 1 field, and the edge pressure barrier is 20 % wider [123]. This is an effect mostly ascribable to the strong decrease in the n_e pedestal height with an almost unvaried width. The minimal amplitude of perturbation field required for an increase in ELM frequency, the so-called ELM mitigation threshold, has a higher value than the density pump-out threshold. In addition, previous JET experimental results also show that the ELM mitigation threshold increased with decreasing q_{95} [116]. Stability analysis of controlled ELMs suggests that the operational point with an n = 1 perturbation field moves from the intermediate-n peeling-ballooning boundary to the low-n peeling boundary, and the radial width of the most unstable mode is reduced from ~3 % down to ~1 % of the normalized minor radius [124].

Compensation of the density pump-out with additional fuelling has been performed during DIII-D ELM suppression experiments. Partial compensation of density pump-out during RMP ELM suppression can be achieved by means of gas puffing. However, strong fuelling with gas puffing or with pellet injection can bring small ELMs back. One example is shown in Fig. 5.11. Thus further optimization of the RMP technique is needed to be able to suppress ELMs fully during pellet fuelled H-mode scenarios for application to ITER [97].

On JET, compensation of the density pump-out has been also investigated using either gas fuelling or pellet injection in low triangularity H-mode plasmas [114, 117, 125]. Although the ELM frequency stays high with n = 1 fields, no recovery of stored energy is observed. An optimized fuelling rate to compensate or the density pump-out effect has been identified, and it depends on the plasma configuration.

5.3.4.4 Non-resonant Magnetic Braking

Plasma rotation braking effects with applied perturbation fields have been observed on DIII-D, NSTX, and JET. It is well known that the plasma rotation is a significant concern for the control of MHD instabilities in a tokamak, because of its stabilizing effects on resistive wall modes [126] and neoclassical tearing modes [127]. Plasma rotation is also important for increasing the field penetration threshold [128], and hence improving the error field tolerance in tokamaks. Therefore, understanding the plasma braking mechanism with an RMP field becomes an important issue for optimising the application of magnetic perturbations.

Neoclassical toroidal viscosity (NTV) theory has been developed to describe the effects of non-axisymmetric magnetic perturbations on the plasma rotation in the collisionless [129] and plateau [130] regimes. Here, the names of the regimes indicate the dependence of the transport on the collisionality (v). The collisionless regime ($\nu/\varepsilon < \sqrt{\varepsilon}/\omega_t$, where ε is the amplitude of the $\cos\theta$ component of the magnetic field, θ is the poloidal angle, $\omega_t = v_t/R_0 q$ is the transit frequency, v_t is the thermal velocity, R_0 is major radius of magnetic axis, and q is the safety factor) can be further divided into two main regimes: the $1/\nu$ regime and the v regime [129]. Determination of $1/\nu$ ($|q\omega_E| < \nu/\varepsilon < \sqrt{\varepsilon}/\omega_t$) and v ($|q\omega_E| > \nu/\varepsilon$) regimes is according to the relationship between the values of the collisionality and $\vec{E} \times \vec{B}$ drift frequency $\omega_E = E_\rho/\rho B_0$ (where E_ρ is the radial electron field, B_0 is the magnetic field strength on the magnetic axis and ρ is the normalized flux-surface label). The breaking of the toroidal magnetic symmetry due to the application of the non-axisymmetric magnetic perturbations causes a nonambipolar radial particle flux and hence the NTV. A generalized analytic solution of NTV and the influence of the NTV torque on the field penetration process has been investigated [131]. A neoclassical 'offset' rotation has been predicted using the NTV theory [129, 132].

Recently, good agreement between the calculated torque from NTV theory in the $1/\nu$ regime and the observed torque induced by the n = 3 fields has been reported on NSTX [133]. The observed rotation damping time on DIII-D was close to the NTV damping time in the 1/v regime, whereas the NTV damping time in the v regime is at least two orders of magnitude larger [134]. However, it was shown that the plasma in DIII-D is mainly in the v regime. An increase in the NTV torque in the v regime has been predicted by including the collisional boundary layer effect (the boundary between the trapped and untrapped particles) [135]. The NTV torque from the boundary layer contribution scales like $\sqrt{\nu}$. The variation of the magnetic field strength should be calculated in the distorted magnetic flux surface [129]. Hence, one should take a Lagrangian variation of the magnetic field strength in NTV torque calculations. It was found that the Lagrangian variation of the magnetic field strength is about one order higher than the Eulerian part [131]. The damping rate of the plasma rotation calculated based on NTV theory using a Lagrangian variation of the magnetic field strength agrees well with that observed on NSTX and DIII-D [136]. The existence of the neoclassical offset rotation with an n = 3 perturbation field was observed on DIII-D [137]. On JET, similar plasma

braking effects have been observed with n = 1 and n = 2 external fields when the same EFCC coil current was applied [125]. The torque profile induced by the n = 1 field has been measured, and it has a global profile. The maximal value of this torque is in the plasma core region and it is about half of the neutral beam injection torque. The calculation shows that the plasma is mainly in the v regime in the plasma core, but is close to the transition between the $1/\nu$ and v regimes. A discrepancy between the observed torque and the torque predicted by NTV theory has been found. Although, both the boundary layer effect and using a Lagrangian variation of the magnetic field strength can reduce this discrepancy. However, the magnitude of the NTV torque calculated in the v regime is still at least one order smaller than the observed one [129, 138].

5.3.4.5 Strike Point Splitting

On MAST, the 3D "manifold" structures, which are induced by an interaction between the applied 3D RMP fields and the 2D plasma equilibrium fields, have been observed using filtered visible imaging [139]. These manifold structures are particularly complex near to the X-point. The manifolds form lobes that are stretched radially both outwards and inwards. Some of these lobes can intersect the divertor target and result in the strike point splitting often observed during RMP experiments [140]. A clear correlation is observed between the size of the lobe length and the change in ELM frequency, which may suggest that the lobes themselves are having a direct impact on the stability of the edge plasma to peeling ballooning modes [141].

Recently, mitigation of type-I ELMs was observed with the application of an n = 2 field in H-mode plasmas on JET with the ILW. In moderate collisionality ($\nu^*_{e,ped} \sim 0.8$) H-mode plasmas, similar to previous results with the C-wall, both an increase in the ELM frequency and density pump-out were observed during the application of the n = 2 field. There are two new observations compared with the C-wall results. Firstly, the effect of ELM mitigation with the n = 2 field was seen to saturate so that the ELM frequency did not further increase above a certain level of n = 2 magnetic perturbations. Secondly splitting of the outer strike point during the ELM crash was seen, resulting in mitigation of the maximal ELM peak heat fluxes on the divertor region.

Splitting of the outer strike point (SP), appearing as multiple peaks in the ELM heat flux profiles measured by a fast IR camera along the outer divertor plate as shown in Fig. 5.14, has been observed during the application of the n = 2 fields on JET with the ILW. Similar findings have been reported on DIII-D in the presence of n = 3 RMP fields [142]. These multiple peaks in the heat flux profile are observed only during a mitigated ELM crash when a certain I_{EFCC} threshold is reached. The preliminary results indicate that this I_{EFCC} threshold for the appearance of splitting of the outer SP during the ELM crash is a similar level as that occurring for the saturation effect of the plasma response.

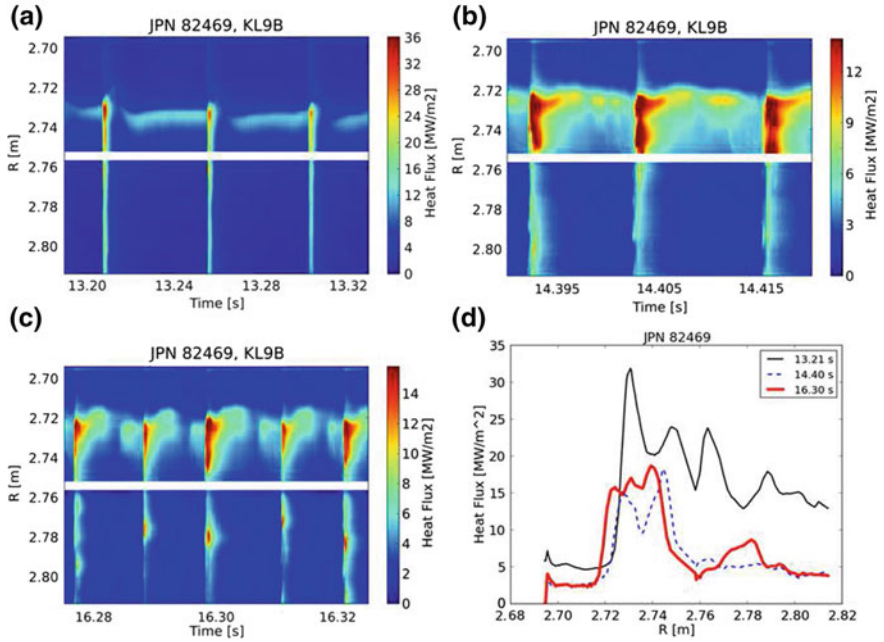

Fig. 5.14 Extended time traces of the heat flux distribution on the outer divertor plate in the phases (*upper left*) without n = 2 field, (*upper right*) with $I_{EFCC} = 44$ kA and (*lower left*) with $I_{EFCC} = 88$ kA. (*lower right*) ELM peak heat flux profiles along the outer divertor. From [112]

5.3.4.6 Multiple Resonances Effects

Multiple resonances in f_{ELM} as a function of the edge safety factor q_{95} have been observed for the first time with an applied low n (= 1, 2) field on the JET tokamak [143, 144]. Without an n = 1 field applied, f_{ELM} increases slightly from 20 to 30 Hz by varying the q_{95} from 4 to 5 in a type-I ELMy H-mode plasma. However, with an n = 1 field applied, a strong increase in f_{ELM} by a factor of 4–5 has been observed with resonant q_{95} values, while the f_{ELM} increased only by a factor of 2 for non-resonant values. The Chirikov parameter calculated using the experimental parameters and the vacuum approximation of the perturbation field indicates that the ergodisation zone may only appear at the far plasma boundary ($\sqrt{\Psi} > 0.95$). The mechanism of edge ergodisation, which is used to explain the results of the ELM suppression with n = 3 fields on DIII-D, may explain the global effect of the n = 1 field on f_{ELM} on JET, but it cannot explain the multi-resonance effect observed with the low n fields. A model, which assumes that the ELM width is determined by a localized relaxation triggered by an unstable ideal external peeling mode, can qualitatively predict the observed resonances when low n fields are applied [145].

5.3.4.7 3D Plasma Displacement

The 3D displacement of the plasma boundary caused by an application of non-axisymmetric perturbation fields has been identified on JET [146], DIII-D [147], AUG [148] and MAST [149]. The empirically observed corrugation of the plasma edge position agrees well with three-dimensional ideal plasma equilibrium reconstruction using the VMEC code [146]. The influence of the 3D corrugation on infinite-n ballooning stability has been examined using the COBRA code [150, 151]. The growth rate of the $n = \infty$ ballooning modes at the most unstable toroidal location is a factor of two larger than in the axisymmetric case i.e. the plasma edge is strongly destabilized at certain toroidal positions [152].

5.3.4.8 Open Questions

To date, many attempts to explain ELM suppression have focused on the idea that the edge thermal and particle losses are enhanced due to the formation of an outer 'ergodic' zone with RMP fields. The 'ergodic' boundary would reduce the edge pressure gradients, and thus stabilize the peeling-ballooning modes thought to underlie ELM formation [73, 153, 154]. This mechanism is mainly supported by two experimental results from DIII-D: (i) splitting of the inner strike-point observed during the RMP ELM suppression phase [155, 156]; and (ii) spin-up of the edge plasma rotation in the co-current direction and changing of the plasma edge electric field to a more positive value due to larger losses of electrons than ions with an ergodic boundary [157]. However, either bulk plasma or diamagnetic rotation [158, 159] can screen the RMP fields from the resonant magnetic flux surfaces. Many calculations of the Chirikov parameter [160] or overlapping of resonant magnetic islands employ a vacuum assumption, which neglects the plasma response (rotational screening effect and equilibrium effect).

Recent experimental results from ELM suppression in Hybrid H-mode plasmas on DIII-D show that small ELMs can appear when the edge safety factor is outside the resonance window or when the H-mode pedestal is perturbed, unrelated to P–B stability [161]. This result indicates that a 3D equilibrium modification may be important for understanding the effect of RMPs on the edge pedestal stability [162]. On the other hand, changes in the edge-plasma profiles during the RMP ELM suppression phase are indicative of a significant alteration in the particle balance with a relatively small change in the energy transport. However, this result can not be explained by stochastic transport theory.

On DIII-D, large Type-I ELMs were also suppressed by n = 3 fields induced by a single row of off-midplane in-vessel coils in plasmas with an ISS at the ITER pedestal collisionality ($\nu_e^* \sim 0.1$), and low edge safety factor ($q_{95} = 3.6$) [163]. The perturbation spectrum induced by a single row of coils is different to that with both upper and lower coils. Based on the results from DIII-D, the correlation of island overlap width and ELM suppression is observed as a useful figure of merit

(Chirikov parameter larger than 1 at $\sqrt{\Psi} \geq 0.925$) to guide the design of the ITER RMP coils [153, 164–168]. The width of the region in the plasma edge with good overlap of the RMP magnetic islands (from vacuum field calculations) is an ordering parameter for the maximum ELM size during the RMP for either RMPs from one row or two poloidally separated rows of internal n = 3 RMP coils, although outliers in the ordering point to important contributions from additional physics mechanisms.

In addition, recent experimental results from both MAST (n = 3, in-vessel off-midplane coils) [106] and JET (n = 1 and 2, external midplane coils) [74] show that ELM suppression is not achieved even with a Chrikov parameter larger than 1 at $\sqrt{\Psi_{pol}} > 0.925$. Those results suggest that ELM suppression using RMPs may also depend on the perturbation spectrum (not only the mode number, but also the ratio of the resonant to the non-resonant components). Although complete ELM suppression at low collisionality with RMPs is only obtained on a single device (DIII-D), the application of RMPs on other machines has either triggered ELMs in otherwise ELM free H-mode periods or increased the ELM frequency in regularly ELM-ing discharges.

Although the mechanism of ELM control with RMPs is not fully understood yet, it has been examined in a wide operational window in many different devices. Further optimisation of the magnetic perturbation with less reduction of the plasma performance and understanding the underlying physics are essential for future investigations.

5.3.4.9 Future RMP ELM Control/Suppression Experiments

The coil systems in different devices employ differing designs, e.g. internal off-midplane coils (DIII-D, MAST) and external midplane coils (JET, MAST, NSTX), and provide different poloidal, m, and toroidal, n, mode number spectra as well as differing radial profiles. Nevertheless, there are common observations like plasma density pump-out and magnetic rotation braking. To date, complete ELM suppression at low collisionality has only been achieved within a narrow operational window of q_{95} by using either n = 2 or 3 fields induced by in-vessel off-midplane coils in DIII-D. Guided by the DIII-D results, a set of ELM control coils has been designed for ITER [153].

To provide a more reliable method for ELM control/suppression, substantial ongoing efforts are presently contributing to two major topics: **the application** and **the physics mechanism**.

- **Application**: This includes (i) the influence of the RMPs on the ELM frequency and size, ELM peak heat loads, plasma confinement; (ii) the operational window, which is defined by the locked mode threshold and the minimal perturbation necessary for an increase in ELM frequency; (iii) rotation braking with magnetic perturbations; (iv) density dump-out compensation; (v) application for ITER-like scenarios.

- **Physics mechanism**: This includes (i) the field penetration process including edge ergodisation, field screening by the plasma rotation and the 3D equilibrium effect; (ii) ELM stability; (iii) Dynamics of edge pedestal profiles; and (iv) multi-resonance effects.

To investigate the physics mechanism of RMP ELM control/suppression, several new RMP coil systems on the world's tokamaks are planned. DIII-D proposes to have 36 new coils (3 rows, and each row has 12 coils) on the inboard wall [120]. This system is very flexible for adjusting the perturbation spectrum. The maximal toroidal mode number of the perturbation fields is 6. When used in combination with the present two rows of coils above and below the outer midplane, the new inboard coils would ultimately allow variation of the RMP radial and poloidal localization plus the capability to separately rotate either $n = 3$ or $n = 4$ RMPs toroidally for tests of field penetration and heat flux spreading models [120]. On EAST, a set of 2×8 ELM control coils including the ability to rotate the perturbation up to $n = 3$ has been installed at the end of 2013. ELM control experiments with $n = 2$, 3 and 4 fields are planned in the coming experimental campaign on EAST. Two rows of internal coils above the mid-plane are being proposed for JET (one with 8 coils, the other with 24) [169]. This system is flexible enough to be able to adjust both the Chirikov parameter and the magnetic perturbation spectrum independently in ITER-relevant scenarios. NSTX is also proposing [170] two rows of internal coils above and below the mid-plane, each one having 12 coils. Feasibility studies of installing in-vessel coils on NSTX and JET are currently ongoing. Future experiments from those devices offer the possibility of examining the underlying mechanism of complete ELM suppression and ELM control.

5.4 New Control Schemes

5.4.1 SMBI ELM Mitigation

ELM mitigation by Supersonic Molecular Beam Injection (SMBI) has been observed on HL-2A [171], KSTAR [172] and EAST [173]. When SMBI cold particles are deposited within the pedestal, consequently, the ELM frequency increases and the ELM amplitude decreases for a finite duration after SMBI. Increases in frequency of $f_{ELM}^{SMBI}/f_{ELM}^{0} \sim 2 - 3.5$ are achieved on HL-2A. In principle, the penetration depth of SMBI is shallower than that of pellet injection, therefore SMBI need not immediately provoke an ELM burst. The results from KSTAR suggest that shallow particle deposition by SMBI changes the local characteristics of the pedestal transport dynamics and the local density profile structure, and consequently alters the ELM dynamics. In addition, pellet injection is highly coherent with individual ELM triggering but the SMBI pulses are not directly correlated with individual ELMs.

5.4.2 ELM Mitigation with Lower Hybrid Waves

Recent results from the Experimental Advanced Superconducting Tokamak (EAST) [174] show that lower hybrid waves (LHWs) provide an effective means of mitigating or suppressing ELMs (seen in Fig. 5.15) by inducing a profound change in the magnetic topology, similar to the effect previously observed with RMPs [112, 155]. This has been demonstrated to be due to the formation of helical current filaments (HCFs) flowing along field lines in the scrape-off layer induced by LHWs. Magnetic perturbations induced by the currents flowing in these edge helical filament structures have been measured by a set of Mirnov coils during the modulation of LHWs. The change in the magnetic topology has been qualitatively modelled by considering the HCFs in a field-line-tracing code. Because of the geometric effect of the LHW antenna, the perturbation fields induced by the HCFs are dominated by the $n = 1$ components. The magnetic perturbation spectrum calculated based on the experimental parameters indicates a good resonant feature, whereby the plasma edge resonant surfaces are well aligned on the ridge of the spectrum. This is consistent with experimental observations of a weak q_{95} dependence of ELM mitigation with LHWs on EAST [175]. This result offers a new attractive means of optimizing the heat load distribution on the divertor plates and suppressing or mitigating the large transient peak heat and particle loads due to ELMs for the next-step fusion reactors (ITER and DEMO).

5.5 Combination of Different Methods

To gain a higher fusion energy production and to secure the plasma first wall components, a fusion device, i.e. ITER, needs to be operated in a high density (close to the Greenwald limit), high edge radiation and steady state small ELM or ELM-free regime. This may need a combination of several different methods of large ELM control/suppression.

On JET, the preliminary experimental results show that the combined application of an $n = 1$ field and vertical kicks ($n = 0$) leads to a reduction of the threshold perturbation level necessary for ELM mitigation to occur [94]. It could reduce the technical difficulty of accessing further high ELM frequency control using a safe size of vertical kicks.

ELM control with a combination of an $n = 1$ field and pellet injection has been demonstrated on JET. The ELM frequency can be increased without any drop in plasma density. During the application of the $n = 1$ field, the ELM frequency increases, even though some of the ELMs are triggered by pellet injection. Further RMP ELM control experiments with a radiating divertor are planned.

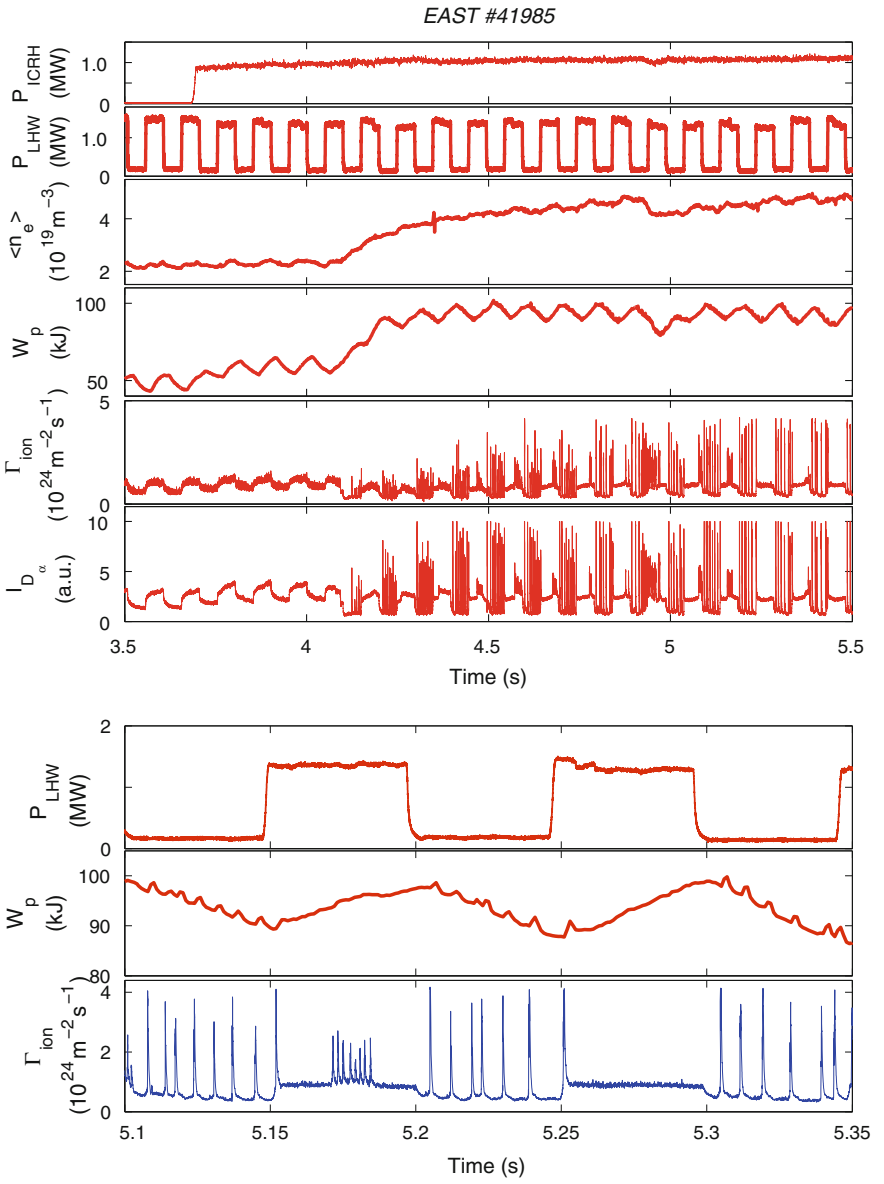

Fig. 5.15 Effect of LHW power modulation on ELMs. The time traces from top to bottom are injected power from ICRH and LHW, central line-averaged density, plasma stored energy, peak particle flux and intensity of D_α emissions in the outer divertor. At the bottom is a focused view of LHW power, stored energy and peak particle flux in the outer divertor. From [174]

5.6 Summary

Erosion and damage caused by large ELMs is one of major hurdles on the route towards achieving magnetic fusion in a reactor scale machine. Scaling predicts that the large ELM energy in ITER will exceed the acceptable level by a factor of ~ 20. Clearly, a reliable ELM control method is needed.

In the past years, several ELM control/suppression methods have been developed. Some important results are summarized below:

- Both experimental and modelling results show that a reduction of ELM energy by impurity seeding is difficult for large ELMs. A combination of radiating divertor with other active ELM control methods is essential for an application to ITER.
- Vertical kicks need in-vessel coils to reach a high kick frequency. Recent results from JET are promising, and this technique will be used for ITER-like wall experiments on JET, in which case the ELM size need only be reduced by a factor of ~ 2–3.
- Pellet pacing can typically achieve a factor of two reduction in the energy per ELM. High frequency ELM pacing still needs to be demonstrated on JET. Indeed, pellet pace-making could assist other ELM control techniques, helping to compensate the density pump-out caused by RMP ELM control/suppression.
- RMP ELM suppression/control has shown very promising results up to now, although the physics mechanism is not well understood as yet. Future joint experiments from different devices (DIII-D, JET, MAST, NSTX, AUG, TCV, KSTAR and EAST) will help us to understand ELM suppression physics and provide support for ITER.

ITER may need a combination of different ELM control methods, many of which are still under active investigation.

References

1. F. Wagner, Phys. Rev. Lett. **49**, 1408 (1982)
2. ITER Physics Basis, Nucl. Fusion **39**, 2137 (1999)
3. J.W. Connor, Plasma Phys. Control. Fusion **40**, 531 (1998)
4. J.A. Snipes, Plasma Phys. Control. Fusion **40**, 765 (1998)
5. W. Suttrop, Plasma Phys. Control. Fusion **38**, 1407 (1996)
6. R.J. Buttery et al., in Proceedings of 22nd EPS Conference on Controlled Fusion and Plasma Physics (Bournrmouth), vol. 19C (1995), p. 273
7. P. Gohil, Phys. Rev. Lett. **61**, 14 (1988)
8. M. Jiang, Plasma Phys. Control. Fusion **54**, 095003 (2012)
9. D.C. McDonald, Fusion Sci. Technol. **53**, 891 (2008)
10. K. Hagashima, T. Shoji, Y. Miura, Nucl. Fusion **36**, 335 (1996)
11. N. Oyama, Nucl. Fusion **44**, 582 (2004)
12. N. Oyama, Nucl. Fusion **45**, 871 (2005)

13. A. Kirk, J. Nucl. Mater. **313**, 1081 (2003)
14. R. Maingi, Nucl. Fusion **45**, 1066 (2005)
15. H. Reimerdes, in Proceedings of 24th EPS Conference on Controlled Fusion and Plasma Physics (Berchtesgaden), vol. 21A (1997), p. 533
16. S. Soldatov, Plasma Phys. Control. Fusion **52**, 085001 (2010)
17. W. Suttrop, Plasma Phys. Control. Fusion **42**, A1 (2000)
18. H. Zohm, Plasma Phys. Control. Fusion **38**, 105 (1996)
19. A. Loarte, Plasma Phys. Control. Fusion **44**, 1815 (2002)
20. A. Loarte, J. Nucl. Mater. **313–316**, 962 (2003)
21. T. Ozeki, Nucl. Fusion **30**, 1425 (1990)
22. J. Stober, Nucl. Fusion **41**, 1123 (2001)
23. M. Bècoulet, Plasma Phys. Control. Fusion **45**, A93 (2003)
24. H.R. Wilson, Plasma Phys. Control. Fusion **48**, A71 (2006)
25. J. Ongena, Plasma Phys. Control. Fusion **43**, A11 (2001)
26. G. Saibene, Plasma Phys. Control. Fusion **44**, 1769 (2002)
27. Y. Kamada, Plasma Phys. Control. Fusion **42**, A247 (2000)
28. Y. Kamada, Plasma Phys. Control. Fusion **44**, A279 (2002)
29. G. Saibene, Nucl. Fusion **45**, 297 (2005)
30. J. Stober, Nucl. Fusion **45**, 1213 (2005)
31. R. Maingi, J. Nucl. Mater. **337–339**, 727–731 (2005)
32. K.H. Burrell, Plasma Phys. Control. Fusion **44**, A253 (2002)
33. W. Suttrop, Plasma Phys. Control. Fusion **45**, 1399 (2003)
34. Y. Sakamoto, Plasma Phys. Control. Fusion **46**, A299 (2004)
35. W. Suttrop, Nucl. Fusion **45**, 721 (2005)
36. K.H. Burrell, Nucl. Fusion **49**, 085024 (2009)
37. M. Greenwald, Phys. Plasma **6**, 1943 (1999)
38. K. Kamiya, Nucl. Fusion **43**, 1214 (2003)
39. N. Oyama, Plasma Phys. Control. Fusion **48**, A171 (2006)
40. E.A. Frieman, Phys. Fluids **16**, 1108 (1973)
41. J.W. Connor, Phys. Plasmas **5**, 2687 (1998)
42. J. Manickam, Phys. Fluids B **4**, 1901 (1992)
43. S.M. Kaye, Nucl. Fusion **30**, 2621 (1990)
44. A.J. Webster, C.G. Gimblett, Phys. Rev. Lett. **102**, 035003 (2009)
45. A.J. Webster, C.G. Gimblett, Phys. Plasmas **16**, 082502 (2009)
46. G.T.A. Huysmans, Plasma Phys. Control. Fusion **47**, 2107 (2005)
47. S. Saarelma, Plasma Phys. Control. Fusion **53**, 025011 (2011)
48. H.R. Wilson, S.C. Cowley, Phys. Rev. Lett. **92**, 175006 (2004)
49. A. Kirk, Plasma. Phys. Control. Fusion **46**, 551 (2004)
50. A. Kirk, Phys. Rev. Lett. **92**, 245002 (2004)
51. A. Kirk, Plasma Phys. Control. Fusion **47**, 315 (2005)
52. A. Schmid, Plasma Phys. Control. Fusion **50**, 045007 (2008)
53. C.C. Hegna, Phys. Plasmas **3**, 584 (1996)
54. S. Saarelma, Plasma Phys. Control. Fusion **48**, 31 (2007)
55. J.W. Connor, R.J. Hastie, J.B. Taylor, Proc. Roy. Soc. London Ser. A Math. Phys. Sci. 365, 1720 (1979)
56. R.L. Miller, R.W. Moore, Phys. Rev. Lett. **43**, 11 (1979)
57. R.L. Miller, Phys. Plasmas **5**, 973 (1998)
58. J. Wesson, Tokamaks, 3rd edn. (Clarendon Press, Oxford, 2004)
59. C.E. Kessel, Nucl. Fusion **34**, 1221 (1994)
60. P.B. Snyder, Phys. Plasmas **9**, 2037 (2002)
61. H.R. Wilson, Phys. Plasmas **9**, 1277 (2002)
62. G.T.A. Huysmans, S.E. Sharapov, A.B. Mikhailovskii, W. Kerner, Phys. Plasmas **8**, 4292 (2001)
63. P.B. Snyder, Nucl. Fusion **44**, 320 (2004)

64. P.B. Snyder, H.R. Wilson, Plasma Phys. Controlled Fusion **45**, 1671 (2003)
65. A. Mossessian, Phys. Plasmas **10**, 1720 (2003)
66. S. Saarelma, Nucl. Fusion **43**, 262 (2003)
67. L.L. Lao, Nucl. Fusion **41**, 295 (2001)
68. T.W. Petrie, J. Nucl. Mater. **196–198**, 848 (1992)
69. O. Gruber, Phys. Rev. Lett. **74**, 4217 (1995)
70. A.W. Leonard, J. Nucl. Mater. **290–293**, 1097 (2001)
71. A.W. Degeling, Plasma Phys. Control. Fusion **45**, 1637 (2003)
72. P.T. Lang, Nucl. Fusion **44**, 665 (2004)
73. T.E. Evans, Nat. Phys. **2**, 419 (2006)
74. Y. Liang, Phys. Rev. Lett. **98**, 265004 (2007)
75. M. Shimada, Progress in the ITER Physics Basis: Chap. 1. Overview Summary Nucl. Fusion 47, S1 (2007)
76. K. Tobita, Nucl. Fusion **49**, 075029 (2009)
77. P. Monier-Garbet, Nucl. Fusion **45**, 1404 (2005)
78. R. Sartori, Plasma Phys. Control. Fusion **46**, 723 (2004)
79. J. Rapp, Nucl. Fusion **44**, 312 (2004)
80. J. Rapp, J. Nucl. Mater. **337–339**, 826 (2005)
81. K. Itami, J. Nucl. Mater. **266–269**, 1097 (1999)
82. S. Sakurai et al., J. Nucl. Mater. **290–293**, 1102 (2001)
83. H. Kubo, Nucl. Fusion **41**, 227 (2001)
84. H. Kubo, JT-60 team. Phys. Plasmas 9, 2127 (2002)
85. S. Higashijima, J. Nucl. Mater. **313–316**, 1123 (2003)
86. J. Rapp, Plasma Phys. Control. Fusion **44**, 639 (2002)
87. G.J. Radford, Contrib. Plasma Phys. **36**, 187 (1996)
88. D. Reiter, H. Kever, G.H. Wolf, Plasma Phys. and Contr. Fus. **33**, 1579 (1991)
89. A. Loarte et al., Fusion energy 2000. in Proceedings of 18th International Conference on Sorrentto (Vienna, IAEA, 2000). CD-ROM file ITERP/11R
90. P.T. Lang, Plasma Phys. Control. Fusion **46**, L31–L39 (2004)
91. F. Sartori, in Proceedings of 35th EPS Conference on Plasma Physics, vol 32D (ECA) (Hersonissos, Greece, 2008), P5.045
92. S.P. Gerhardt, Nucl. Fusion **50**, 064015 (2010)
93. E. de la Luna et al., in Proceedings of 36th EPS Conference on Plasma Physics (Sofia) (ECA), vol. 33E (2009), P5.174
94. E. de la Luna et al., 23rd IAEA, EXC/8-4 (2010)
95. P.T. Lang, Nucl. Fusion **43**, 1110 (2003)
96. P.T. Lang, Nucl. Fusion **47**, 754 (2007)
97. L.R. Baylor et al., in Proceedings of 35th EPS Conference on Plasma Physics (Hersonissos, Greece) (ECA), vol. 32D (2008), P4-098
98. A.R. Polevoi, Nucl. Fusion **43**, 1072 (2003)
99. D.K. Mansfield, Nucl. Fusion **53**, 113023 (2013)
100. L.R. Baylor, in Proceedings 37th EPS Conference on Plasma Physics and Controlled Fusion (Dublin, Ireland, 2010), P2.117 http://ocs.ciemat.es/EPS2010PAP/pdf/P2.117.pdf
101. G.T.A. Huysmans, Plasma Phys. Control. Fusion **51**, 124012 (2009)
102. F.M. Poli, Nucl. Fusion **50**, 025004 (2010)
103. G. Kocsis, Nucl. Fusion **47**, 1166 (2007)
104. S.K. Combs, J. Vac. Sci. Tech. A **6**, 1901 (1988)
105. L.R. Baylor, Nucl. Fusion **49**, 085013 (2009)
106. A. Kirk, Nucl. Fusion **50**, 034008 (2010)
107. J.M. Canik, Nucl. Fusion **50**, 034012 (2010)
108. T.E. Evans, Phys. Rev. Lett. **92**, 235003 (2004)
109. T.E. Evans, Nucl. Fusion **48**, 024002 (2008)
110. W. Suttrop, Phys. Rev. Lett. **106**, 225004 (2011)
111. Y.M. Jeon, Phys. Rev. Lett. **109**, 035004 (2012)

112. Y. Liang, Nucl. Fusion **53**, 073036 (2013)
113. W. Suttrop et al., in Proceedings of 39th EPS Conference & 16th International Congress on Plasma Physics (2012), P2.092
114. Y. Liang, Nucl. Fusion **50**, 025013 (2010)
115. I. Barlow, Fusion Eng. Des. **58–59**, 189 (2001)
116. Y. Liang, Plasma Phys. Control. Fusion **49**, B581 (2007)
117. Y. Liang, J. Nucl. Mater. **390–91**, 733–739 (2009)
118. S. Jachmich, J. Nucl. Mater. **390–391**, 768–772 (2009)
119. H.R. Koslowski et al., in 34th EPS Conference on Plasma Physics Warsaw 2-6 July 2007, ECA, vol. 31F (2007), P-5.135
120. M.E. Fenstermacher et al., 23rd IAEA, ITR/P1-30 (2010)
121. J.M. Canik, Nucl. Fusion **50**, 064016 (2010)
122. J.C. Vallet, Phys. Rev. Lett. **67**, 2662 (1991)
123. A. Alfier, Nucl. Fusion **48**, 115006 (2008)
124. S. Saarelma, Plasma Phys. Control. Fusion **51**, 035001 (2009)
125. Y. Liang, Plasma Fusion Res. **5**, S2018 (2010)
126. E.J. Strait, Phys. Rev. Lett. **74**, 2483 (1995)
127. R. Buttery, Phys. Plasmas **15**, 056115 (2008)
128. R. Fitzpatrick, Phys. Plasmas **5**, 3325 (1998)
129. K.C. Shaing, Phys. Plasmas **10**, 1443 (2003)
130. K.C. Shaing, Phys. Fluids **29**, 521 (1986)
131. J.-K. Park, Phys. Rev. Lett. **102**, 065002 (2009)
132. A.J. Cole, Phys. Plasmas **15**, 056102 (2008)
133. W. Zhu, Phys. Rev. Lett. **96**, 225002 (2006)
134. M. Bècoulet, Nucl. Fusion **49**, 085011 (2009)
135. K.C. Shaing, Phys. Plasmas **15**, 082506 (2008)
136. J.-K. Park, Phys. Plasmas **16**, 056115 (2009)
137. A.M. Garofalo, Phys. Rev. Lett. **101**, 195005 (2008)
138. Y. Sun, Plasma Phys. Control. Fusion **52**, 105007 (2010)
139. A. Kirk, Phys. Rev. Lett. **108**, 255003 (2012)
140. A. Kirk, Nucl. Fusion **53**, 043007 (2013)
141. I.T. Chapman, Nucl. Fusion **52**, 123006 (2012)
142. M. Jakubowski, Nucl. Fusion **49**, 095013 (2009)
143. Y. Liang, Phys. Rev. Lett. **105**, 065001 (2010)
144. Y. Liang, Nucl. Fusion **51**, 073001 (2011)
145. C.G. Gimblett, R. J. Hastie, P. Helander, Phys. Rev. Lett. 96, 035006-1-4 (2006)
146. I.T. Chapman, Nucl. Fusion **47**, L36 (2007)
147. R. Moyer, Nucl. Fusion **52**, 123019 (2012)
148. R. Fischer, Plasma Phys. Control. Fusion **54**, 115008 (2012)
149. I.T. Chapman, Plasma Phys. Control. Fusion **54**, 105013 (2012)
150. S.P. Hirshman, D.K. Lee, Comput. Phys. Commun. **43**, 143 (1986)
151. W.A. Cooper, Comput. Phys. Commun. **180**, 1524 (2009)
152. R.J. Sanchez, Comp. Physics **161**, 576 (2000)
153. M.J. Schaffer, Nucl. Fusion **48**, 024004 (2008)
154. M. Bècoulet, Nucl. Fusion **48**, 024003 (2008)
155. M. Jakubowski, PRL **96**, 035004 (2006)
156. O. Schmitz, Plasma Phys. Control. Fusion **50**, 124029 (2008)
157. K. Burrell, Plasma Phys. Control. Fusion **47**, B37 (2005)
158. M. Heyn, Nucl. Fusion **48**, 024005 (2008)
159. R. Fitzpatrick, Nucl. Fusion **33**, 1049 (1993)
160. B.V. Chirikov, Phys. Rep. **52**, 263 (1979)
161. B. Hudson, Nucl. Fusion **50**, 045006 (2010)
162. Park Jong-kyu, Phys. Rev. Lett. **99**, 195003 (2007)
163. M.E. Fenstermacher, Nucl. Fusion **48**, 122001 (2008)

164. M.E. Fenstermacher, J. Nucl. Mater. **390–391**, 793–796 (2009)
165. T.E. Evans, Phys. Plasmas **13**, 056121 (2006)
166. M.E. Fenstermacher, Phys. Plasmas **15**, 056122 (2008)
167. R.A. Moyer, Phys. Plasmas **12**, 056119 (2005)
168. R.A. Moyer, Nucl. Fus. **45**, 595 (2005)
169. C.G. Lowry, Bull. Am. Phys. Soc. **54**, 329 (2009)
170. NSTX Research 5-Year Plan for 2009-13, http://nstx.pppl.gov/fiveyearplan.html
171. W.W. Xiao, Nucl. Fusion **52**, 114027 (2012)
172. Kim Jayhyun, Nucl. Fusion **52**, 114011 (2012)
173. X.L. Zou et al. in Proceedings of 24th IAEA Fusion Energy Conference October 8–13, PD/P8-08 (IAEA, San Diego, 2012)
174. Y. Liang, Phys. Rev. Lett. **110**, 235002 (2013)
175. J.G. Li et al., 17 NOVEMBER 2013. Nat. Phys. DOI:10.1038/NPHYS2795